



Uncertainty Quantification and Sensitivity Analysis for Computational FFR Estimation in Stable Coronary Artery Disease

FREDRIK E. FOSSAN ¹, JACOB STURDY ¹, LUCAS O. MÜLLER,¹ ANDREAS STRAND,¹ ANDERS T. BRÅTEN,^{2,3} ARVE JØRGENSEN,^{3,4} RUNE WISETH,^{2,3} and LEIF R. HELLEVIK¹

¹Department of Structural Engineering, Norwegian University of Science and Technology, Trondheim, Norway; ²Clinic of Cardiology, St. Olavs Hospital, Trondheim, Norway; ³Department of Circulation and Medical Imaging, Norwegian University of Science and Technology, Trondheim, Norway; and ⁴Department of Radiology and Nuclear Medicine, St. Olavs Hospital, Trondheim, Norway

(Received 27 June 2018; accepted 12 October 2018)

Associate Editors Dr. David A. Steinman, Dr. Francesco Migliaavacca, and Dr. Ajit P. Yoganathan oversaw the review of this article.

Abstract

Purpose—The main objectives of this study are to validate a reduced-order model for the estimation of the fractional flow reserve (FFR) index based on blood flow simulations that incorporate clinical imaging and patient-specific characteristics, and to assess the uncertainty of FFR predictions with respect to input data on a per patient basis.

Methods—We consider 13 patients with symptoms of stable coronary artery disease for which 24 invasive FFR measurements are available. We perform an extensive sensitivity analysis on the parameters related to the construction of a reduced-order (hybrid 1D–0D) model for FFR predictions. Next we define an optimal setting by comparing reduced-order model predictions with solutions based on the 3D incompressible Navier–Stokes equations. Finally, we characterize prediction uncertainty with respect to input data and identify the most influential inputs by means of sensitivity analysis. **Results**—Agreement between FFR computed by the reduced-order model and by the full 3D model was satisfactory, with a bias ($\text{FFR}_{3\text{D}} - \text{FFR}_{1\text{D}-0\text{D}}$) of $-0.03 (\pm 0.03)$ at the 24 measured locations. Moreover, the uncertainty related to the factor by which peripheral resistance is reduced from baseline to hyperemic conditions proved to be the most influential parameter for FFR predictions, whereas uncertainty in stenosis geometry had greater effect in cases with low FFR. **Conclusion**—Model errors related to solving a simplified reduced-order model rather than a full 3D problem were small compared with uncertainty related to input data. Improved measurement of coronary blood flow has the potential to reduce uncertainty in computational FFR predictions significantly.

Keywords—Computational FFR, Uncertainty quantification, Model complexity, Total uncertainty.

INTRODUCTION

Ischemic heart disease is the leading cause of death globally,⁵¹ and its relevance will increase as the global population ages. In this study we consider patients with stable coronary artery disease (CAD) which, in addition to acute myocardial infarction, is the main symptomatic manifestation of CAD. In this context, fractional flow reserve (FFR) has been shown to be a reliable invasive tool to study the functional significance of coronary artery stenoses. In fact FFR is currently the gold standard for diagnosis of hemodynamic significance of coronary stenoses and is calculated as the ratio between cardiac cycle averaged pressures distal (\bar{P}_{distal}) and proximal ($\bar{P}_{\text{proximal}}$) to a stenosis, namely

$$\text{FFR} = \frac{\bar{P}_{\text{distal}}}{\bar{P}_{\text{proximal}}}. \quad (1)$$

FFR is acquired invasively by simultaneous measurement of both pressures during drug induced hyperaemia (maximum coronary flow). $\bar{P}_{\text{proximal}}$ is measured by a guiding catheter while \bar{P}_{distal} is obtained with a sensor-tipped pressure wire. FFR-guided revascularization has improved event-free survival and lowered healthcare costs in randomized studies.^{7,33,48} Even though major clinical guidelines recommend the use of FFR, it is measured in less than 1/3 of interventions according to a study performed in the USA.¹⁵ The primary reasons reported were lack of time, unavailability of trained interventionalists and the relatively high cost of the procedure. Over the last decade many attempts have been made to predict FFR non-inva-

Address correspondence to Fredrik E. Fossan, Department of Structural Engineering, Norwegian University of Science and Technology, Trondheim, Norway. Electronic mail: fredrik.e.fossan@ntnu.no

sively using computational fluid dynamics and mathematical models.⁶ The ultimate goal of such efforts has been to provide the medical community with a readily available, cheap and non-invasive quantification of FFR.

Seeking clinical applicability, many proposed methods for non-invasive FFR prediction rely on simplified versions of the original physical problem, i.e. simplifications to the original problem are made in order to reduce computational cost and to allow for a fast calculation of FFR, for example.^{19,34} However, in such studies, no information on the errors made by using simplified models are provided. Two notable exceptions are found in Refs. 2 and 3, where results obtained using reduced, one-dimensional (1D) blood flow models are validated by comparison to results obtained using three-dimensional (3D) transient models for a synthetically generated population and for a real patient population, respectively. However, in both cases the impact of modelling assumptions chosen to simplify the problem is either only partially explored or completely ignored. We perform an extensive evaluation of the impact of model reduction choices on FFR predictions by using uncertainty quantification and sensitivity analysis (UQ&SA) tools. These tools are extremely useful in addressing such questions, as UQ&SA provide insight into which elements of the simplified model are most influential on FFR prediction and are thus ideal candidates for optimization.

A few previous studies have investigated the sensitivity of FFR predictions to various sources of uncertainty in patient-specific models of coronary flow,^{29,40} while others have analyzed generic models of coronary blood flow and stenoses as general investigations into the uncertainty of model predicted FFR.^{9,47} Sankaran *et al.*⁴⁰ and Morris *et al.*²⁹ both investigated the effects of uncertainty in computational prediction of FFR. Sankaran *et al.* accounted for uncertainties in lesion geometry, peripheral resistance and blood viscosity, while Morris *et al.* considered uncertainty about parameters for a lumped stenosis model, proximal pressure, and resistance in the coronary microvasculature.

This study extends the above mentioned previous works by considering all sources of uncertainty studied in previous works and by additionally including uncertainty in the percentage of flow to a specific coronary branch. Furthermore, by performing such a study on a population of patient-specific cases, we provide further insight into the role played by different parameters for different ranges of FFR, with particular attention to intermediate stenoses with FFR values between 0.7 and 0.9, and show how

the various sources of uncertainty may impact individual cases differently.

The rest of this paper is structured as follows. In the “**Materials and Methods**” section we introduce a predictive model of FFR based on a reduced-order, hybrid 1D, zero-dimensional (0D) blood flow model. Additionally we describe the UQ&SA framework in the “**Uncertainty Quantification and Sensitivity Analysis**” section, with which we perform two different analyses. The first is performed as a step in the development and validation of the reduced-order model, and the second studies the effect of input parameters on FFR predictions. Next, in the “**Results**” section we present results for the optimal reduced-order model setup, as well as for the UQ&SA analysis performed on FFR predictions. Finally, in the “**Discussion**” section we discuss our findings as well as considerations on further steps to be taken in order to increase the accuracy and reduce the uncertainty in model-based FFR prediction.

MATERIALS AND METHODS

Study Population

We consider a population of 13 patients that underwent invasive angiography and FFR measurement(s) after clinical and coronary computed tomography angiography (CCTA) examinations indicated stable CAD. From these patients a total of 24 FFR measurements were collected, i.e. some patients had more than one suspected stenosis. The FFR measurements had a mean of 0.77 and a standard deviation of 0.17, with a positive FFR prevalence of 41.67% for a cutoff value of $FFR < 0.8$. The patients were recruited as part of an ongoing clinical trial at St. Olavs Hospital, Trondheim, Norway.⁴ See Table 7 for a summary of population characteristics and Table 12 for all available data for each FFR measurement.

Recruitment

The study subjects included in the analysis had undergone CCTA due to chest pain and suspicion of stable CAD. Patients were enrolled with the findings of at least one coronary stenosis at CCTA examination and being further referred for invasive coronary angiography (ICA) with invasive FFR measurements.

Exclusion criteria included unstable CAD, previous percutaneous coronary intervention or bypass surgery, renal insufficiency (estimated glomerular filtration rate < 30), obesity (BMI > 40), non diagnostic quality of the CCTA due to motion artifacts or known allergy to contrast agent or contraindications to adenosine.

Data Acquisition

Medical Data Acquisition

CCTA was performed using two CT scanners with 2×128 detector rows (Siemens dual source Definition Flash) using a standardized protocol.¹⁴

Echocardiographic imaging was performed using a GE Vivid E95 scanner (GE Vingmed Ultrasound, Horten, Norway). Cardiac output (CO) was calculated based on cross-sectional area of left ventricle outflow tract measured immediately proximal to the points of insertion of the aortic leaflets and velocity time integral derived from PW Doppler.

FFR was measured using Verrata Plus (Philips Volcano, San Diego, USA) pressure wires according to standard practice. Intra-coronary nitroglycerin (0.2 mg) was given to all patients before advancing the pressure wire into the coronary arteries and hyperemia was induced by continuous intravenous infusion of adenosine at a rate of at least $140 \mu\text{g/kg/min}$. Pressure was measured over several cardiac cycles and FFR measurements were taken during the nadir (lowest observed value) of the $\bar{P}_{\text{distal}}/\bar{P}_{\text{proximal}}$ ratio. After measurement the interventional cardiologist removed the pressure wire back to the equalization point at the tip of the guiding catheter, to ensure that there was no drift.

Standard non-invasive diastolic/systolic pressure measurements (P_{meas}) were performed on both arms as part of clinical routine before ICA using an automatic, digital blood pressure device, Welch Allyn ProBP 3400.

Coronary Vessel Segmentation and Volume Meshing

Segmentation of vessels was performed using the open-source software ITK-SNAP,⁵⁴ which provides a user-friendly interface for a semi-automatic active contour evolution segmentation approach. The output of ITK-SNAP is a labeled voxel volume identifying segmented vessels and a surface mesh of the segmented volume (in VTK format). Surface mesh processing, addition of flow extensions and meshing were performed using the open-source library Vascular Modeling ToolKit (VMTK).^{1,46} The 3D volume meshes form the basis for both the reference 3D model and the reduced-order model. For the latter, additional processing is necessary as described in the “[From a 3D Domain to a 1D Network](#)” section. For 3D simulations, the meshing refinement level was determined by a meshing algorithm parameter called edge-length factor l_f , which was set to $l_f = 0.21$ for all simulations. A mesh independence study showed that such discretization provides mesh independent FFR predictions for a set of four patient-specific geometries.

Reduced-Order Model

In this section we present a steady state reduced-order (1D–0D) model for FFR prediction that incorporates clinical imaging and patient-specific characteristics.

Mathematical Model

1D blood flow in steady state conditions in terms of pressure and flow (P , Q) is modeled as

$$\frac{\partial Q}{\partial x} = 0, \quad (2a)$$

$$\frac{\partial}{\partial x} \left(\frac{Q^2}{A} \right) = -\frac{A}{\rho} \frac{\partial P}{\partial x} + \frac{f}{\rho}, \quad (2b)$$

where $f = -2(\zeta + 2)\mu\pi U$ is the frictional term, $\rho = 1050 \text{ kg/m}^3$ is the density, $\mu = 0.0035$ is the viscosity of blood and $U = Q/A$ is the cross-sectional averaged velocity. The cross-sectional area A is assumed constant and equal to the area obtained from the segmentation of medical images. The velocity profile is prescribed by

$$u(x, \zeta, t) = U(x, t) \frac{\zeta + 2}{\zeta} \left[1 - \left(\frac{\zeta}{r} \right)^\zeta \right], \quad (3)$$

where $r(x, t)$ is the lumen radius, ζ is the radial coordinate and ζ is the polynomial order.

At arterial connections, conservation of mass and a coupling equation for pressure are enforced, i.e.

$$\sum_{i=1}^N Q_i = 0, \quad (4a)$$

$$P_1 + \lambda \frac{\rho}{2} U_1^2 = P_i + \lambda \frac{\rho}{2} U_i^2 + \Delta P_i \quad i = 2, \dots, N, \quad (4b)$$

where N is the number of vessels in the connection, ΔP is an additional pressure loss and λ is a coefficient that can assume values between zero and one. At healthy junctions, ΔP is set to zero and λ is set to one, so that Eq. (4b) describes continuity of total pressure. At arterial stenoses the assumptions from which the 1D model is derived do not hold. Therefore, stenotic regions are removed from the computational domain and the coupling relation between the upstream and downstream healthy segments is modeled with Eqs. (4a)–(4b) by setting $N = 2$, $\lambda = 0$ and where ΔP is obtained from the experimentally derived stenosis model presented in Ref. 53. Here we use an equivalent expression, reported in Ref. 25, namely

$$\Delta P = \frac{K_v \mu}{A_0 D_0} Q + \frac{K_t \rho}{2 A_0^2} \left(\frac{A_0}{A_s} - 1 \right)^2 Q |Q|, \quad (5)$$

where A_0 and A_s refer to cross-sectional areas of the normal and stenotic segments, respectively. Similarly, D_0 and D_s represent the normal and stenotic diameters, whereas L_s is the length of the stenosis. Furthermore, K_v and K_t are empirical coefficients, with $K_v = 32(0.83 L_s + 1.64 D_s) \cdot (A_0/A_s)^2/D_0$ and $K_t = 1.52$.²⁵

Parameters of the 1D–0D model are summarized in Table 1. Note that ζ and K_t are studied as part of the construction of the reduced-order model (see “UQ&SA for 1D–0D Model Setting” section), whereas ρ and μ are studied in the UQ&SA for FFR prediction setting (see “UQ&SA for FFR Prediction Setting” section).

Numerical Solution

Integration of Eqs. (2a) and (2b) along the length of a vessel segment yields

$$Q_{\text{in}} = Q_{\text{out}}, \quad (6a)$$

$$P_{\text{in}} + \frac{\rho}{2} \left(\frac{Q_{\text{in}}}{A_{\text{in}}} \right)^2 = P_{\text{out}} + \frac{\rho}{2} \left(\frac{Q_{\text{out}}}{A_{\text{out}}} \right)^2 + Q_{\text{in}} \int_0^l \frac{2(\zeta + 2)\pi\mu}{A^2} dx, \quad (6b)$$

where l is the length of the 1D segment, while subscripts in and out denote variables at the inlet and outlet of the segment, respectively.

In this work we perform simulations considering two different settings. In the first setting, flows are prescribed at all outlets and pressure is prescribed at the network’s inlet, whereas for the second setting we consider prescribed pressure at the inlet and terminal resistances attached to each outlet. As noted below, the use of two settings is motivated by the different features of the two UQ&SA analyses described in the “Uncertainty Quantification and Sensitivity Analysis” section.

Prescribed inlet pressure and outlet flows. The solution to this problem requires traversal of the network from outlets to inlet in order to determine the flow in each vessel of the network. Subsequently, the pressure

in each vessel is computed by traversing from the network’s inlet and evaluating Eqs. (6a), (6b), and coupling conditions Eqs. (4a) and (4b) for each vessel and junction. Note that the solution procedure is also valid in the limiting case of one arterial segment. We use this solution procedure in the analysis related to the construction of the reduced-order model described in the “UQ&SA for 1D–0D Model Setting” section, where the coronary networks are split into individual segments and where boundary-conditions are obtained from the 3D solutions.

Prescribed inlet pressure and resistances attached to outlets. Consider now a bifurcating network of V vessels with L outlets and N internal nodes or bifurcations. In this case, instead of prescribing flow, we attach a terminal resistance R_j , with $j = 1, 2, \dots, L$, to each outlet. The unknowns now are $\mathbf{x} = [Q_{\text{out},1}, Q_{\text{out},2}, \dots, Q_{\text{out},L}]$, and L nonlinear equations are provided by

- The i th bifurcation with N_d^i daughters provides $N_d^i - 1$ equations like Eq. (4b), yielding $L - 1$ equations. Note that two-vessel junctions and in particular vessels coupled by stenoses do not provide equations.
- The missing equation is provided by the prescribed inlet pressure: $P_{\text{in},k} - P_{\text{in}}^{\text{presc}} = 0$, where $P_{\text{in},k}$ is the pressure at the inlet of the k th vessel, and $P_{\text{in}}^{\text{presc}}$ is the prescribed pressure at the inlet of the network.

While for the case of prescribed inlet pressure and outlet flow the solution to the problem is trivial, the case of resistances attached to outlets requires solving a nonlinear problem. In fact, equations can be written as a nonlinear algebraic system of equations, $\mathbf{f}(\mathbf{x}) = 0$. The Python routine `scipy.optimize.minimize.root`²² was used to solve the nonlinear system. Note that each evaluation of $\mathbf{f}(\mathbf{x})$ requires solving a problem similar to the one where flows are prescribed at outlets, but where the tree is traversed from the outlets towards the inlet and where coupling condition Eq. (4b) is only enforced between the parent vessel and one (arbitrarily chosen) daughter vessel. After convergence Eq. (4b) will be fulfilled for all vessels that share a bifurcation node. We use this solution procedure in the analysis related to UQ&SA for FFR prediction setting described in the “UQ&SA for FFR Prediction Setting” section.

From a 3D Domain to a 1D Network

The construction of a network of 1D domains from the original 3D domain involves a series of non-trivial steps that are described in detail in the following section. The methods illustrated in this section are a modification of those proposed in Ref. 2. All steps

TABLE 1. Parameters of the 1D–0D model (see “Mathematical Model” section).

Symbols	Description
ρ	Density
μ	Viscosity
ζ	Velocity profile parameter
K_t	Expansion coefficient
K_v	Viscous coefficient

described here were performed using VMTK¹ and VTK⁴¹ libraries via Python scripting.

Skeletonization of the 3D domain. In order to obtain the 1D network, centerlines of the 3D volume meshes are generated and cross-sectional areas, A_i , with normal vector aligned to centerline tangent vector at node i are calculated. Spacing between centerline nodes is approximately 0.5 mm. From A_i we calculate the radius of the cross-sectional area, $r_i = \sqrt{\frac{A_i}{\pi}}$, while the length of each vessel segment is calculated by summing the Euclidean distance between centerline points. The intrinsic coordinate, x , is defined in a similar manner, where we have that $x_i = \sum_{n=1}^i \Delta S_{n-1,n}$, where $S_{n-1,n}$ is the Euclidean distance between centerline point $n-1$ and n .

Masking of junctions. After centerline generation, the portions of the centerlines which coincide with arterial junctions are masked in order to exclude them from the 1D domain definition, since no reasonable 1D description of such portions of the domain can be formulated. See Appendix 1 for details.

Masking of stenotic regions. Stenotic regions are parts of the original domain where the 1D blood flow model is not valid and must be replaced by *ad hoc* models for the prediction of pressure drops across stenoses. Such regions are detected and quantified by comparing the observed radius, r_i , to an estimated healthy radius, \hat{r}_i , predicted by a weighted Gaussian kernel filtering procedure on the radius, r_i . The healthy radius is required by the stenosis detection algorithm since *a priori* there is no reference radius available to characterize the stenosis degree. The methodology followed here was proposed by Shahzad *et al.*⁴²

First a local average radius, r_i^{\max} , is calculated by averaging the observed radii according to a Gaussian kernel with standard deviation σ_{\max} , that is

$$r_i^{\max} = \frac{\sum_{i'=1}^n N(i'|i, \sigma_{\max}) r_{i'}}{\sum_{i'=1}^n N(i'|i, \sigma_{\max})}. \quad (7)$$

Here and in, what follows $i|i$ denotes the intrinsic distance between centerline nodes with indexes i and i' . Based on this smoothed radius and its deviation from the local average, a weight factor is calculated for each observed radius as

$$w_i = N(r_i | r_i^{\max}, \sigma_r). \quad (8)$$

Finally, the healthy radius is estimated by averaging the observed radii weighted by proximity, using a Gaussian kernel with standard deviation σ_x , and the likelihood, w_i , of each observed radius, r_i , given the local average, r_i^{\max} , i.e.

$$\hat{r}_i = \frac{\sum_{i'=1}^n N(i'|i, \sigma_x) w_{i'} r_{i'}}{\sum_{i'=1}^n N(i'|i, \sigma_x) w_{i'}}, \quad (9)$$

where $N(i'|i, \sigma) = \frac{1}{\sigma\sqrt{2\pi}} \exp\{-\frac{(i' - i)^2}{2\sigma^2}\}$.

A centerline node is marked as a stenosis if the stenosis degree is above a stenosis threshold, θ_s , where stenosis degree is defined as

$$SD_i = 1 - \frac{r_i}{\hat{r}_i}. \quad (10)$$

Stenotic regions are determined by traversing upstream and downstream from the centerline nodes where $SD_i > \theta_s$ and marking all nodes where SD_i is above a certain healthy stenosis threshold, θ_h . The radius associated with centerline points at the start (upstream, u) and end (downstream, d) are used to calculate the reference radius of the stenotic region according to $r_0 = 0.5(r_u + r_d)$. The stenosis model [see Eq. (5)] is then parameterized by the minimum radius, r_s , reference radius, r_0 and stenosis length, L_s , computed as the distance between nodes u and d along the centerline, see Algorithm 1.

Algorithm 1 Stenosis detection algorithm

- 1: Estimate healthy radius \hat{r} of 1D segment
 - 2: Calculate SD for all points in segment
 - 3: Create set P of points $\{x_i | SD_i > \theta_s\}$
 - 4: **while** P is not empty **do**
 - 5: Remove the first item x_i from P
 - 6: $x_u \leftarrow \arg \min(x_i - x_j)$ such that $SD_j < \theta_h$
 - 7: $x_d \leftarrow \arg \min(x_j - x_i)$ such that $SD_j < \theta_h$
 - 8: Remove x_p from P if $u < p < d$
 - 9: $r_s \leftarrow \infty$
 - 10: **for** $k = u \dots d$ **do**
 - 11: **if** $r_k < r_s$ **then**
 - 12: $r_s \leftarrow r_k$
 - 13: $l_s \leftarrow x_d - x_u$
 - 14: $r_0 \leftarrow 0.5(r_u + r_d)$
 - 15: Replace the region between x_u and x_d with a stenotic junction model (see Eq. (5)) with parameters r_s , r_0 , and l_s
-

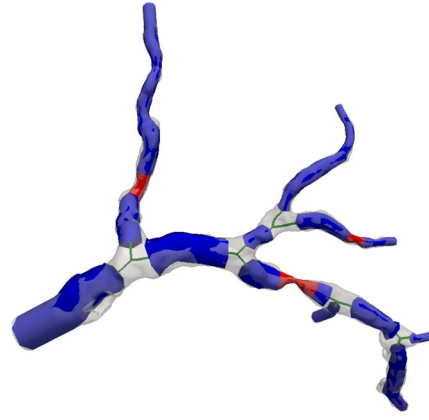
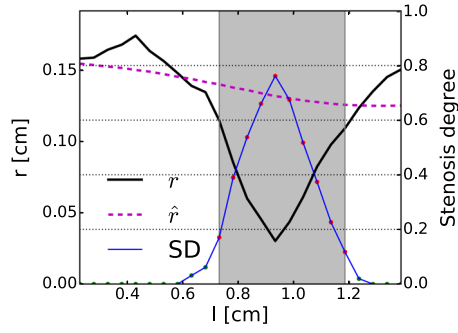


FIGURE 1. Original radius, r , and estimated healthy radius, \hat{r} , together with stenosis degree, SD, and the stenotic region (shaded area) for a 1D segment is shown in the left panel. A 1D network of arteries extracted from a 3D volume mesh (transparent grey), where junctions and stenotic regions have been masked is illustrated in the right panel.

TABLE 2. Summary of stenosis detection parameters (see “From a 3D Domain to a 1D Network” section).

Symbols	Description
σ_x^*	Local averaging kernel length
σ_r^*	Healthy radius variability
σ_{\max}^*	Healthy smoothing kernel length
θ_s	Stenosis threshold
θ_h^*	Healthy stenosis threshold

In the original work by Shahzad *et al.*⁴² centerline dimensions are given in millimeters, and σ_x , σ_r and σ_{\max} were set to 8, 0.25 and 200 mm respectively. In this work we have related the parameters to the maximum radius, $\max(r_i)$, of the vessel of interest such that $\sigma_x = \max(r_i) \sigma_x^*$, $\sigma_r = \max(r_i) \sigma_r^*$ and $\sigma_{\max} = \max(r_i) \sigma_{\max}^*$. Furthermore, θ_h is constrained to be less than or equal to θ_s by $\theta_h = \theta_h^* \theta_s$, where $0 \leq \theta_h^* \leq 1$.

The determination of stenotic regions is illustrated in Fig. 1. The left panel shows the original radius, r , together with the estimated healthy radius, \hat{r} , for a 1D segment. Additionally, the calculated stenosis degree and a stenotic region based on a stenosis threshold, $\theta_s = 0.3$, and healthy threshold, $\theta_h = 0.2$, are shown. The right panel of the figure shows a 1D network extracted from a 3D volume mesh for one of the patients included in this study. The 1D segments are separated at arterial junctions, and further divided into stenotic (red) and healthy regions (blue), as described above. The segment with the most severe stenosis corresponds to the vessel shown in the left panel of the figure.

The parameters related to stenosis detection are summarized in Table 2, and all of them are studied as part of the construction of the reduced-order model (see “UQ&SA for 1D–0D Model Setting” section).

TABLE 3. Percentage of CO to a coronary branch, λ_{cor} as a function of branch type and dominance, adapted from Sakamoto *et al.*³⁷

	Right dominance	Left dominance
Left branch	2.6	3.4
Right branch	1.9	0.9

Definition of Patient-Specific Parameters for Simulations

Simulations performed in this work require the determination of parameters from patient-specific data. These parameters and the procedures for personalizing them are described in the following.

Baseline coronary flow. In this work we perform individual simulations of the left or right coronary branch depending on the site of lesion/measurement. The flow to a specific branch is based on the work of Sakamoto *et al.*,³⁷ who studied coronary blood flow to the left and right branches in relation to coronary artery dominance. They report mean and standard deviation of absolute flow to each coronary branch but do not account for variability due to differences in CO or total coronary flow. Thus, the reported absolute flows and standard deviations are normalized by the population average CO, 6L/min, in order to produce the corresponding flow fractions, λ_{cor} , as given in Table 3. With this, the baseline coronary flow to a specific branch is

$$q_{\text{cor}} = \lambda_{\text{cor}} \text{CO}_{\text{meas}}, \quad (11)$$

where measured CO, CO_{meas} , was available for each patient, as explained earlier in this section.

Mean arterial pressure. Mean arterial pressure (MAP) is computed via the widely used formula³⁶

$$\text{MAP} = \frac{2}{3}\text{DBP} + \frac{1}{3}\text{SBP}. \quad (12)$$

Diastolic blood pressure (DBP) and systolic blood pressure (SBP) were obtained non-invasively as explained earlier in this section. MAP is prescribed at the inlet of the computational domain.

Coronary resistance. Total peripheral resistance for a given branch is estimated from MAP and the target branch flow in baseline conditions as

$$R_{\text{tot}} = \frac{\text{MAP} - P_d}{q_{\text{cor}}}, \quad (13)$$

where $P_d = 5 \text{ mmHg}$ is the outflow/venous pressure.

The total peripheral resistance, R_{tot} is distributed among outlets using Murray's law,³¹ that is

$$R_j = \frac{\sum_{i=1}^{N_{\text{out}}} r_i^c}{r_j^c} R_{\text{tot}}, \quad (14)$$

where j refers to the j th outlet of the network, and c is Murray's exponent. In order to match average branch flow, q_{cor} defined in Eq. (11), total peripheral resistance is modified to account for resistance within the computational domain. Starting with the initial guess provided by Eq. (13), the reduced-order model is solved and R_{tot} is updated according to

$$R_{\text{tot}}^{m+1} = R_{\text{tot}}^m (1 - \omega(q_{\text{cor}} - q_{\text{obs}})/q_{\text{cor}}), \quad (15)$$

where m is the iteration index, q_{obs} is the observed flow at the branch inlet and $\omega = 0.9$ is a relaxation parameter. Once a new value for R_{tot} is available, the resistance is distributed among outlets using Eq. (14).

Coronary flow can increase significantly with respect to resting flow during hyperemic conditions. Vasodilation of peripheral vessels downstream from epicardial arteries is the most important mechanism controlling coronary flow.⁴⁵ Such changes can be seen as variations in the total coronary resistance index (TCRI), α . We model the effect of vasodilation of

peripheral coronary arteries by dividing R_{tot} by such a factor

$$R_{\text{tot,hyp}} = R_{\text{tot}}/\alpha. \quad (16)$$

The patient-specific parameters previously introduced are summarized in Table 4. Note that CO, λ_{cor} , MAP, c and α are studied in the UQ&SA for FFR prediction setting (see “UQ&SA for FFR Prediction Setting” section).

Modeling Pipeline

For a given patient-specific dataset, the pipeline for the reduced-order model FFR prediction is as follows:

- (1) Definition of 3D domain *via* ITK-SNAP segmentation of CCTA images.
- (2) Preparation of computational domain through meshing and centerline extraction.
- (3) Transformation of the 3D domain to a 1D network and identification of junctions and stenotic regions.
- (4) Baseline simulation using parameters defined in the “Definition of Patient-Specific Parameters for Simulations” section: total peripheral resistance R_{tot} for a given branch is modified in order to match target branch flow q_{cor} defined by Eq. (29).
- (5) In order to mimic hyperemic conditions, total branch resistance is reduced: $R_{\text{tot,hyp}} = R_{\text{tot}}/\alpha$, and is subsequently distributed among outlets with criteria specified in Eq. (32).
- (6) Computational FFR is calculated based on the results of the hyperemic simulation as $P_{\text{distal}}/\text{MAP}$, where P_{distal} is the pressure distal to a given stenosis.

The pipeline is illustrated schematically in Fig. 2.

Three-Dimensional Simulations

3D simulations are used to develop and validate the reduced-order model proposed in this work in two ways. First, we perform transient and steady state 3D simulations for all 13 patients in order to verify that the steady state regime is accurate enough to model hyperemic blood flow in coronary arteries. Second, steady state solutions are used as reference results to optimize reduced-order model parameters. We use results from 3D simulations since we want to analyze to effect of modeling assumptions and corresponding errors related to the transformation of the original 3D problem into a 1D-0D problem. By using reference 3D simulations with equivalent boundary conditions we are able to isolate such errors, as would not be the case if the comparison had been made directly with invasive

TABLE 4. Summary of patient-specific parameters discussed in the “Definition of Patient-Specific Parameters for Simulations” section.

Symbols	Description
CO_{meas}	Cardiac output
λ_{cor}	Percentage of cardiac output to a coronary branch
MAP	Mean arterial pressure
SBP	Systolic blood pressure
DBP	Diastolic blood pressure
P_d	Outflow/venous pressure
c	Murray's exponent
α	Total coronary resistance index

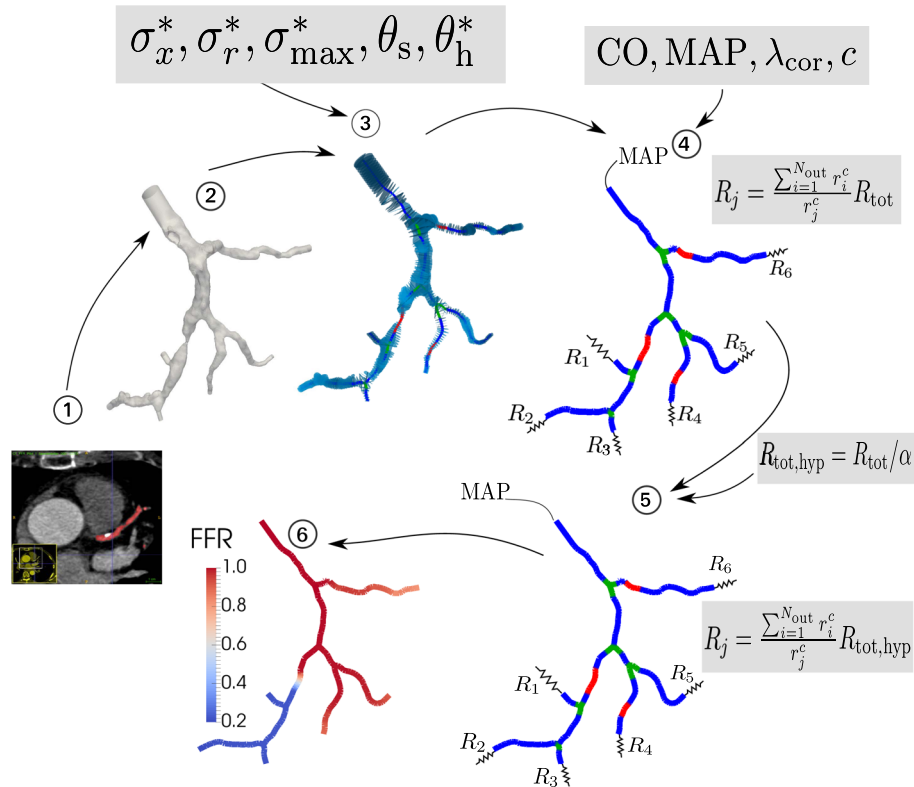


FIGURE 2. Illustration of the modeling pipeline. (1) coronary artery segmentation, (2) preparation of computational domain, (3) transformation of the 3D domain to a 1D network and identification of junctions and stenotic regions, (4) incorporation of clinical data and performing baseline/resting simulations, (5) hyperemic simulation and (6) post-processing and extraction of computational FFR. See “Modeling Pipeline” section for additional descriptions of the different steps, and “From a 3D Domain to a 1D Network” and “Definition of Patient-Specific Parameters for Simulations” sections for detailed description of steps 3 and 4/5 respectively.

pressure measurements. 3D simulations are performed on segmented coronary trees treated as rigid domains with a prescribed pressure as inlet boundary condition and Windkessel models attached to each network outlet. A full description of the underlying mathematical models and their numerical treatment is provided in [Appendix 2](#).

Uncertainty Quantification and Sensitivity Analysis

The patient-specific modelling paradigm attempts to enhance clinically measured data by predicting unmeasured physiological states through model simulations based on available data and validated modelling principles. As clinical data always has some uncertainty and unmeasured parameters may be known to vary significantly, we must characterize the uncertainty of model predictions in addition to verifying that a computational model solves the idealized mathematical model to an adequate level of accuracy. Towards this end we employ UQ&SA to assess the uncertainty present in patient-specific model predictions as well as to identify inputs that prevent greater certainty in model predictions.

In this study we perform two UQ&SA cases using Monte Carlo and polynomial chaos approaches (see [Appendix 3](#) for an outline of the framework used in this paper, which is based on the review of Eck *et al.*⁹). First we perform an assessment of the variability of the individual pressure drop in each segment of all vessel networks considered in this study to identify which model parameters are most able to influence the resulting pressure drop, thus allowing prioritization of which parameters to estimate from the data. Subsequently, we assess the uncertainty of the final 1D–0D predictions of FFR given the uncertainties in clinical data.

First we briefly summarize notation. UQ&SA typically analyzes a model prediction y as a function M of inputs \mathbf{z} , $y = M(\mathbf{z})$, where lower case letters denote the relationship of a deterministic case where \mathbf{z} is known. Uncertain inputs are denoted \mathbf{Z} as they are random variables and thus $Y = M(\mathbf{Z})$ is also a random variable.

As the most commonly used measures in SA, Sobol Indices,³⁹ is based on scalar variables, we extend the ideas of Eck *et al.*¹⁰ to summarize the sensitivities over all measurement locations and across patients. Eck

*et al.*¹⁰ proposed a method to summarize sensitivities of time varying quantities by weighting the sensitivities by the uncertainty, $\mathbb{V}[Y]$, at each time point. This may naturally be extended to any set or region where a summary of the sensitivities is desired. First we evaluate the portion of variance of an output (k) attributable to the particular input (i):

$$V_i^k = \mathbb{V}[\mathbb{E}[Y_k | Z_i]] = S_i^k \mathbb{V}[Y_k], \quad (17a)$$

$$V_{T,i}^k = \mathbb{E}[\mathbb{V}[Y | \mathbf{Z}_{-i}]] = S_{T,i}^k \mathbb{V}[Y_k], \quad (17b)$$

where the vector, \mathbf{Z}_{-i} , contains all elements of \mathbf{Z} except Z_i , and S_i^k and $S_{T,i}^k$ are the first order and total sensitivity index of output Y_k with respect to Z_i . In contrast to S_i and $S_{T,i}$, V_i^k and $V_{T,i}^k$ allow to perform a comparison based on the absolute amount of uncertainty due to input Z_i for each output rather than on the normalized proportion. Finally, from V_i^k and $V_{T,i}^k$ the averaged first-order sensitivity indices are calculated as

$$AS_i = \frac{\sum_{k=1}^n V_i^k}{\sum_{k=1}^n \mathbb{V}[Y_k]} = \frac{\sum_{k=1}^n S_i^k \mathbb{V}[Y_k]}{\sum_{k=1}^n \mathbb{V}[Y_k]}, \quad (18)$$

and averaged total sensitivity indices are

$$AS_{T,i} = \frac{\sum_{k=1}^n V_{T,i}^k}{\sum_{k=1}^n \mathbb{V}[Y_k]} = \frac{\sum_{k=1}^n S_{T,i}^k \mathbb{V}[Y_k]}{\sum_{k=1}^n \mathbb{V}[Y_k]}. \quad (19)$$

These may provide useful summaries of sensitivities, particularly when the uncertainties of the various outputs of M are quite different.

UQ&SA for 1D–0D Model Setting

In order to identify the most relevant parameters in the construction of the reduced-order model described in the “[Reduced-Order Model](#)” section we perform a sensitivity analysis with respect to the parameters $\mathbf{Z}_{3D \rightarrow 1D} = [\zeta, \sigma_x^*, \sigma_r^*, \sigma_{\max}^*, \theta_s, \theta_h^*, K_t]$. Parameter variability is described by using uniform distributions with limits based on the plausible ranges of each parameter (see Table 5 for exact ranges). Sensitivity analysis is performed individually for all ($N = 248$) 1D segments (including three or

more centerline points), and with $y = M(\mathbf{z}) = \Delta P_{1D-0D}(\mathbf{z}_{3D \rightarrow 1D})$. The flow rate and inlet pressure for each segment are taken from the solution obtained using the 3D modeling framework. Finally, ΔP_{1D-0D} is calculated by applying the solution procedure where inlet pressure and outlet flows are prescribed, as described in the “[Numerical Solution](#)” section.

Measures of uncertainty and sensitivity were estimated by the Monte Carlo method as described by Saltelli,³⁸ and the accuracy of UQ&SA results were assessed by evaluating the standard deviation of the estimates from 10 bootstrapped samples³⁵ until the standard deviation was below 0.0033 (i.e. 99% confident that obtained value is within ± 0.01 , with assumptions of normality) for all sensitivity indices with an estimated value larger than 0.05. The maximum number of model evaluations was 3,121,812.

UQ&SA for FFR Prediction Setting

Conducting blood flow simulations for estimation of FFR as described in the “[Reduced-Order Model](#)” section requires the determination of parameters based on clinical imaging, patient-specific characteristics, clinical measurements and values from literature (population-based studies, physiological studies, *etc.*). We conduct UQ&SA to understand the effects of uncertainty in the input parameters, $\mathbf{Z}_{FFR} = [\text{CO}, \text{MAP}, \lambda_{\text{cor}}, c, \alpha, H, \Delta r_s, \lambda_{L_s}]$ (see Table 6), on FFR predictions for all available (24) invasive FFR measurements. In the following we discuss the basis for the chosen distribution of \mathbf{Z}_{FFR} in this UQ&SA study.

A standard deviation in DBP of 5.5 mmHg and a standard deviation in SBP of 3.3 mmHg were reported in Ref. 17. By assuming perfect positive correlation between DBP and SBP, a standard deviation in the estimated aortic pressure is 4.77 mmHg. By these considerations, we model the estimate of MAP as a normal variable with mean given by Eq. (12) and with a standard deviation of 4.77 mmHg.

Dubin *et al.*⁸ compared echocardiographic estimates of CO to thermodilution-derived invasive estimates. The average difference between the two methods was

TABLE 5. Ranges for exploratory sensitivity analysis of the hybrid 1D–0D model (“[Reduced-Order Model](#)” section).

Input	Symbols	Minimum	Maximum
Flow profile order	ζ	2	9
Local averaging kernel length	σ_x^*	0.1	3
Healthy radius variability	σ_r^*	0.0075	1.5
Healthy smoothing kernel length	σ_{\max}^*	3	8
Diseased threshold	θ_s	0	1
Healthy threshold	θ_h^*	0	1
Turbulent loss coefficient	K_t	1	2

Uniform distributions with minimum and maximum values denoted below are assigned to all parameters. All parameters are dimensionless.

TABLE 6. Input uncertainties for evaluation of the effects of parametric input uncertainty on 1D–0D estimates of FFR.

Input	Branch, dominance	Symbols	Distribution
Cardiac output	–	CO (L/min)	$N(\text{CO}_{\text{meas}}, 0.69)$
Arterial pressure	–	MAP (mmHg)	$N(P_{\text{meas}}, 4.77)$
Coronary flow fraction	Left, right	λ_{cor} (%)	$U(1.78, 3.42)$
Coronary flow fraction	Right, right	λ_{cor} (%)	$U(1.1, 2.7)$
Coronary flow fraction	Left, left	λ_{cor} (%)	$U(2.7, 4.1)$
Coronary flow fraction	Right, left	λ_{cor} (%)	$U(0.27, 1.6)$
TCRI	–	α (–)	$G(3, 0.75)$
Murray's law exponent	–	c (–)	$U(2.0, 3.0)$
Hematocrit	–	H (–)	$N(0.45, 0.031)$
Stenosis radius perturbation	–	Δr_s (mm)	$U(-0.1, 0.1)$
Stenosis length factor	–	λ_{L_s} (–)	$U(-0.2, 0.2)$

Uniform distributions are denoted by $U(\text{min}, \text{max})$ and normal distributions $N(\text{mean}, \text{std. dev.})$. The gamma distribution for α is denoted by $G(\text{shape}, \text{scale})$. The measured cardiac output is denoted CO_{meas} . Mean aortic pressure is represented as P_{meas} , and it is obtained from measurements and Eq. (12). We include coronary flow fraction distributions for each of the four possible combinations of branch and dominance, but note that only one is used for any given case.

0.11 L/min with a standard deviation of 0.69 L/min. Thus, the uncertainty in CO based on the measurement, CO_{meas} , is modeled by a normally distributed random variable with mean corresponding to the PW Doppler estimate of CO_{meas} and a standard deviation of 0.69 L/min.

The percent of flow to a specific coronary branch, λ_{cor} is based on the work of Sakamoto *et al.*³⁷ as explained in the “[Definition of Patient-Specific Parameters for Simulations](#)” section. Incorporating their reported values on variability we obtain the distributions of flow fractions as given in Table 6.

Blood density and viscosity are related to the hematocrit level. We adopt the relation for viscosity reported in Sankaran *et al.*,⁴⁰ where $\mu = \frac{\mu_p}{(1-H)^{2.5}}$, with viscosity of plasma $\mu_p = 0.001$ and hematocrit level H . With this we model H as a normal variable with a mean of 0.45 and a standard deviation of 0.031 based on average population variations.⁵⁰ The density of blood can be related to the hematocrit according to $\rho = \rho_e H + (1 - H)\rho_p$, where $\rho_p = 1018 \text{ kg/m}^3$ is the density of plasma, and $\rho_e = 1085 \text{ kg/m}^3$ is the density of erythrocytes.²³

In our modeling framework, the total peripheral resistance is distributed among outlets using Murray's law,³¹ which has a theoretical exponent of $c = 3$, derived from the principle of minimum work. More recent studies have suggested an exponent of $c = 7/3$,¹⁸ and we thus consider Murray's exponent to be a uniform variable with values between 2.0 and 3.0.

The coronary arteries are segmented semi-automatically from CT images using ITK-SNAP. The software requires one to set upper and lower thresholds for intensities (Hounsfield units) that define what is considered coronary vessel lumen. A larger lower

threshold will decrease the cross-section of the segmented lumen, whereas a smaller lower threshold will have the contrary effect. Such variations in lumen cross-section are particularly important at stenotic regions. To account for this, we introduce a global parameter, Δr_s , to be applied to all stenotic regions of a network such that the minimum radius in stenotic regions is given by $r_s = r_{s,\text{segmented}} + \Delta r_s$, where $r_{s,\text{segmented}}$ is the minimum radius as obtained from the original segmentation. The minimum $r_{s,\text{segmented}}$ in our population is 0.29 mm, and we model Δr_s as a uniform variable ranging from -0.1 to 0.1 mm. Similarly, we model the stenotic length as $L_s = (1 + \lambda_{L_s})L_{s,\text{segmented}}$, where λ_{L_s} is assumed to follow a uniform distribution between -0.2 and 0.2 .

Although TCRI is difficult to measure, it is related to the coronary flow reserve (CFR), which is the ratio of flow in hyperemic and baseline conditions. According to the meta-analysis by Johnson *et al.*,²¹ CFR is normally between 1 and 6 with an average value of 2.57 for non-ischemic vessels. The distribution is akin that of the gamma.²⁸ From these considerations, we model the hyperemic factor α as a gamma distribution with shape parameter 3, scale-factor 0.75 and shifted to 1.

We perform UQ&SA for FFR predictions from the reduced-order model described in the “[Reduced-Order Model](#)” section for 24 locations where FFR was measured invasively. Parameters that are related to the process of going from a 3D problem to a 1D–0D model are those deriving from the sensitivity analysis described in the “[UQ&SA for 1D–0D Model Setting](#)” section and an optimization procedure based on such analysis. The pipeline for predicting FFR is the same as outlined in the “[Modeling Pipeline](#)” section, however, now with the input parameters \mathbf{Z}_{FFR} as de-

scribed above and summarized in Table 6. Numerical solutions are obtained by applying the solution procedure where inlet pressure is prescribed and resistances are attached to outlets, as described in the “Numerical Solution” section.

The Python package chaospy¹² was used to calculate polynomial chaos approximations of model predicted FFR. Regression was used to estimate the coefficients of the approximations for model evaluations at points sampled according to the Hammersley sequence, which allows for adaptively increasing the number of samples evaluated. The number of points used for each order of approximation was twice the number of terms in the expansion. The accuracy of the results from UQ&SA was assessed by comparing the estimates between successive orders of approximation until the difference between estimated sensitivity indices was below 0.01 for all indices with an estimated value larger than 0.05. Approximation of maximum order 7 was performed, which required 12,870 samples.

Cases that required approximation order greater than 7 were computed more efficiently in terms of computational burden by the Monte Carlo method as described by Saltelli,³⁸ and the accuracy of UQ&SA results was assessed by evaluating the standard deviation of the indices from 10 bootstrapped samples³⁵ until the standard deviation was below 0.0066 (i.e. 99% confident that obtained value is within ± 0.02 , with assumptions of normality) for all sensitivity indices with an estimated value larger than 0.05. The maximum number of model evaluations was 1,775,970.

RESULTS

Patient Characteristics

Table 7 provides an overview of general patient characteristics, invasive FFR measurements and quantitative coronary angiography. Full information about each patient as well as all FFR measurements used in this study are provided in Appendix 4. Moreover, Figures 13, 14 and 15 in Appendix 4 display the geometry of all coronary trees considered. These figures also include the location of distal pressure measurements used for the computation of FFR.

Design and Validation of the Reduced-Order Model for Coronary Blood Flow Simulations

Sensitivity Analysis

We performed sensitivity analysis as described in the “UQ&SA for 1D-0D Model Setting” section in order to identify most influential parameters, $\mathbf{Z}_{3D \rightarrow 1D} = [\zeta, \sigma_x^*, \sigma_r^*, \sigma_{\max}^*, \theta_s, \theta_h^*, \mathbf{K}_t]$, in the construction of the

TABLE 7. Study population characteristics.

Characteristics	Units	Datum
Generic data		
No. of male patients	Datum (percentage)	13 (69)
Age	Years	57.5 (10.2)
Height	cm	175.4 (9.3)
Weight	kg	85.8 (13.5)
Body mass index	kg/cm ²	27.8 (3.1)
MAP	mmHg	101.5 (10.9)
CO	L/min	5.0 (0.9)
CAD risk factor	Datum (percentage)	
Diabetes		1 (8)
Hypertension		7 (54)
Dyslipidemia		2 (15)
Smoking		2 (15)
Previous CAD events		0 (0)
Invasive FFR measurements		
FFR	–	0.77 (0.17)
LAD artery	Datum (percentage)	12 (48)
RCA	Datum (percentage)	6 (24)
LCX artery	Datum (percentage)	4 (16)
Diagonals	Datum (percentage)	2 (8)
RPDA	Datum (percentage)	1 (4)
Quantitative invasive angiography		
Sensitivity	Percentage	56
Specificity	Percentage	87
Positive predicted values	Percentage	71
Negative predicted values	Percentage	76

Results are reported as “value(standard deviation)” unless otherwise specified. *LAD* left anterior descending, *RCA* right coronary artery, *LCX* left circumflex, *RPDA* right posterior descending artery.

reduced-order model described in the “Reduced-Order Model” section. The sensitivity analysis was performed for each of the 248 coronary vessel segments to estimate first-order (S_i) and total ($S_{T,i}$) sensitivity indices for each case. The average sensitivities for all cases are presented in Table 8 and show that the velocity-profile parameter ζ is by far the most influential parameter for most of the cases, with an average $S_{T,\zeta}$ of 0.88. The second most influential parameter is θ_s , which determines the marking of stenotic regions and has an average S_{T,θ_s} of 0.13. Moreover, aggregated sensitivities, AS_i and $AS_{T,i}$, where the individual uncertainties, $\mathbb{V}[Y]$, are taken into account are also shown in Table 8 and show that weighting the sensitivities with the uncertainty leads to a different ranking in terms of most influential parameters. The stenosis threshold is the parameter that contributes the most aggregate sensitivity, with $AS_{T,\theta_s} = 0.65$. Second most influential is σ_x^* , followed by ζ and θ_h^* .

The results from the sample based sensitivity analysis described in the “UQ&SA for 1D-0D Model Setting” section were also analyzed in terms of the residuals $res = \Delta P_{3D} - \Delta P_{1D-0D}(z)$. In particular, cases where no realization of $\Delta P_{1D-0D}(z)$ in the broad

TABLE 8. Summary of sensitivities resulting from the analysis in the “UQ&SA for 1D–0D Model Setting” section.

	ζ	σ_x^*	σ_r^*	σ_{\max}^*	θ_s	θ_h^*	K_t
S_i	0.87 (0.22)	0.01 (0.02)	0.00 (–)	0.00 (–)	0.07 (0.14)	0.00 (0.01)	0.00 (–)
$S_{T,i}$	0.88 (0.22)	0.04 (0.07)	0.02 (0.03)	0.00 (–)	0.13 (0.20)	0.02 (0.03)	0.01 (0.01)
AS_i	0.16	0.12	0.01	0.00	0.47	0.03	0.02
$AS_{T,i}$	0.17	0.28	0.06	0.01	0.65	0.09	0.03

The average first-order (S_i) and total ($S_{T,i}$) sensitivity indices [see Eqs. (37a) and (37b)], and the uncertainty weighted first-order (AS_i) and total ($AS_{T,i}$) sensitivity indices are reported [see Eqs. (18) and (19)]. Both average and weighted sensitivities were averaged over all 248 vessel segments. Standard deviations are given in parentheses where applicable, and cases with standard deviation below 0.01 are denoted with a dash.

range defined by $\mathbf{Z}_{3D \rightarrow 1D}$ yielded residuals lower than 7.5 mmHg were inspected in detail. Such segments were either associated with a moderate to severe stenosis with non-cylindrical shape and abrupt changes in radius, i.e., calcified stenosis, or multiple mild stenoses with non-cylindrical shape.

Identification of Optimal Parameters

We performed optimization to estimate the values of the four most influential parameters ($\theta_s, \sigma_x^*, \zeta$ and θ_h^*) according to $AS_{T,i}$. The remaining parameters were fixed: $\sigma_r^* = 1$, $\sigma_{\max}^* = 4$ and $K_t = 1.52$. We used the Python package `scipy` to perform parameter estimation. A grid search approach, `scipy.optimize.brute`, was chosen due to the discontinuous character of the problem in terms of stenosis identification and inability of other algorithms to provide meaningful results. In order to enhance identifiability we separated the optimization into two cohorts, one in which the parameters related to the stenosis detection were estimated, and one in which ζ was optimized. In the first cohort ($N = 19$ vessel segments), all vessel segments with $V_{T,\theta_s}^k > 1$ mmHg [see Eq. (17b)] were included, i.e. vessel segments where the square root of the variance due to θ_s contributed to 1 mmHg or more. In the second cohort ($N = 213$ vessel segments), all vessel segments with $V_{T,\theta_s}^k < 0.1$ mmHg were included and used to estimate ζ . The root mean square error was used as cost function in the parameter optimization, defined as

$$\epsilon = \sqrt{\frac{1}{N} \sum_{k=1}^N (\Delta P_{3D}^k - \Delta P_{1D-0D}^k)^2} \quad (20)$$

with N the number of vessel segments in the optimization procedure, ΔP_{3D}^k the pressure drop in vessel segment k obtained with the 3D model, and ΔP_{1D-0D}^k the pressure drop obtained using the 1D–0D model. Optimized parameters are shown in Table 9, and Fig. 3 shows predicted FFR from the 1D–0D model (applying optimized parameters) vs. predicted FFR

TABLE 9. Optimal parameters for 1D–0D model settings.

Parameter	ζ	σ_x^*	σ_r^*	σ_{\max}^*	θ_s	θ_h^*	K_t
Optimal/default value	4.31	2.32	1	4	0.13	0.90	1.52

Estimated values are indicated in bold. All parameters are non-dimensional.

from the 3D model framework at locations where FFR was measured. Equivalent inlet (pressure) and outflow (resistance) boundary conditions were employed as defined in Appendix 2. The mean difference between FFR_{3D} and FFR_{1D-0D} was -0.03 and the standard deviation was 0.03. Indeed, the two worst residuals were associated with vessel segments with non-cylindrical shape and abrupt changes in radius, as identified through analysis of residuals (see previous section).

UQ&SA for FFR Prediction

Sensitivity Analysis

We performed UQ&SA with respect to the uncertain input parameters $\mathbf{Z}_{FFR} = [\text{CO}, \text{MAP}, \lambda_{\text{cor}}, c, \alpha, H, \Delta r_s, \lambda_{L_s}]$ at 24 locations where FFR was measured invasively, as described in the “UQ&SA for FFR Prediction Setting” section. Average first-order (S_i) and total ($S_{T,i}$) sensitivity indices are summarized in Table 10 together with weighted first-order (AS_i) and total ($AS_{T,i}$) sensitivity indices. Both sets of indices indicate that uncertainties due to inlet pressure, MAP, Murray’s exponent, c , and stenosis length, λ_{L_s} , have low influence on predicted FFR for the studied population, model framework, and assumed input uncertainties. Only the indices of α , H and Δr_s vary significantly between the two sets, where the sensitivity of Δr_s increases when the uncertainty in model output, $\mathbb{V}[Y]$ is taken into account. The contrary is valid for H . In other words, the uncertainty in FFR is lower in the cases where H has a high influence as compared with

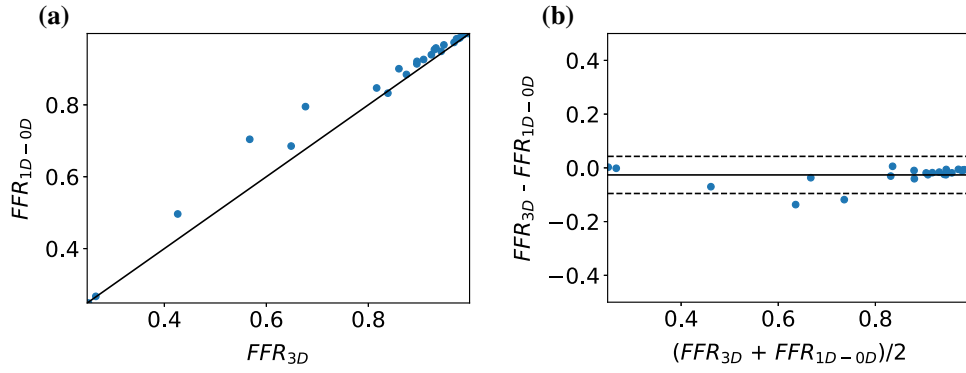


FIGURE 3. Comparison of FFR_{1D-0D} and FFR_{3D} . Scatter plot (left) and Bland–Altman plot (right). The reduced-order model had a bias of $FFR_{3D} - FFR_{1D-0D} = -0.03$ and a standard deviation of 0.03.

TABLE 10. Summary of sensitivities resulting from the analysis in the “UQ&SA for FFR Prediction Setting” section.

	CO	MAP	λ_{cor}	C	α	H	Δr_s	λ_{L_s}
S_i	0.07 (0.03)	0.01 (–)	0.15 (0.07)	0.00 (–)	0.45 (0.14)	0.08 (0.11)	0.17 (0.18)	0.00 (–)
$S_{T,i}$	0.09 (0.03)	0.01 (–)	0.18 (0.07)	0.00 (–)	0.51 (0.14)	0.09 (0.13)	0.19 (0.20)	0.00 (–)
AS_i	0.08	0.00	0.13	0.00	0.40	0.02	0.34	0.00
$AS_{T,i}$	0.09	0.00	0.14	0.00	0.42	0.02	0.36	0.00

The average first-order (S_i) and total ($S_{T,i}$) sensitivity indices [see Eqs. (37a) and (37b)], and the uncertainty weighted first-order (AS_i) and total ($AS_{T,i}$) sensitivity indices are reported [see Eqs. (18) and (19)]. Both average and weighted sensitivities were averaged over all 24 locations where FFR was measured in the clinic. Standard deviations are reported in parentheses, and cases with standard deviation below 0.01 are denoted with a dash.

cases where Δr_s has a high influence. The hyperemic factor α is the most influential parameter according to both sets of sensitivity indices, followed by the uncertainty in minimum radius, Δr_s . Sensitivity indices are also visualized in the top row of Fig. 4, where averaged sensitivity indices for all 24 locations are considered. The bottom row of the same figure shows average and weighted sensitivity indices for cases ($N = 11$) where FFR was in the critical region $0.7 < FFR_{meas} < 0.9$. The most significant difference is seen in sensitivity to Δr_s , which is lower when only FFR values in this range are considered. The standard deviation of the average first-order and total sensitivity indices are also indicated through the vertical error bars in Fig. 4. As can be seen, α , H and Δr_s have particular high standard deviations, i.e. the value of these sensitivity indices varies a lot from case to case.

The top part of Fig. 5 shows the effect of uncertainty in input parameters on predicted FFR in terms of the mean $\mathbb{E}[Y]$ (blue circles) together with the 95% prediction interval for all measured locations. The FFR obtained from the 3D framework and 1D–0D model with equivalent inflow and outflow boundary conditions are also shown for comparison. In the bottom part of the figure parameters CO, λ_{cor} and α are fixed at their nominal values. The horizontal lines represent \pm two standard deviations

(std. dev. = 0.02) of repeated FFR measurements,²⁰ i.e. 95% probability of a FFR measurement error smaller than this under assumption of normality.

DISCUSSION

Validation of the 1D–0D Modeling Framework for FFR Prediction

In this study we have presented a framework for conducting blood flow simulations for estimation of FFR based on clinical imaging and patient-specific characteristics. Furthermore, two different modeling approaches were considered. The first approach is based on the transient/steady state 3D incompressible Navier–Stokes equations in rigid domains. 3D simulations were performed to confirm that steady state simulations can accurately reproduce FFR predictions (see Appendix 2) and also used as a reference in the development of the second model considered, namely the hybrid 1D–0D model. Here, healthy segments are modeled using the 1D equations for blood in axisymmetric arteries, and stenotic regions are modeled by an experimentally derived model for stenosis.²⁵ Fully 1D or even 1D–0D models for FFR prediction have been previously proposed in the literature.^{2,3} However, this study is distinct in that we consider a fast steady state

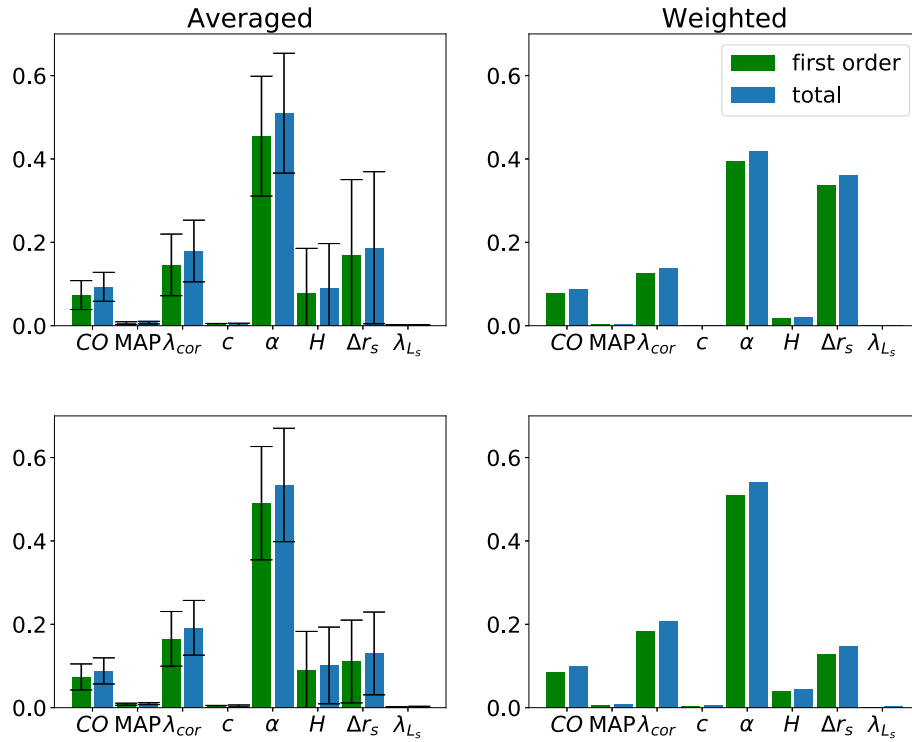


FIGURE 4. The average first-order (S_i) and total ($S_{T,i}$) sensitivity indices [see Eqs. (37a) and (37b)], and the uncertainty weighted first-order (AS_i) and total ($AS_{T,i}$) sensitivity indices are reported [see Eqs. (18) and (19)]. The top two bar-plots represent sensitivities when all 24 cases were considered, whereas in the bottom two, only cases ($N = 11$) where FFR was in the critical region $0.7 < FFR_{meas} < 0.9$ were considered. The standard deviation of the first-order (S_i) and total ($S_{T,i}$) sensitivity indices are also indicated through the vertical error bars.

version of the model and perform an extensive sensitivity analysis focusing on the model parameters that are related to the model reduction (i.e. going from a 3D to a simplified 1D–0D problem). We considered two parameters associated with necessary assumptions in the 1D–0D equations, namely the radial dependence of the velocity profile, represented by ζ in Eq. (2b) and the parameter K_t associated with the pressure drop due to a sudden expansion. In addition, five parameters related to the detection and quantification of stenotic regions were considered. This preprocessing of the 3D domain is necessary in order to separate the coronary tree into healthy segments where the assumptions of 1D equations for blood flow are sufficiently accurate, and stenotic regions where the assumptions do no longer hold and stenoses models have to be used.

Through the SA of given input parameters $\mathbf{Z}_{3D \rightarrow 1D}$ we found that the velocity profile parameter, ζ , was the most influential parameter. This is natural since most vessel segments were relatively smooth, and thus the stenosis detection algorithm and its associated parameters will not influence the predicted pressure drop. The other parameters under consideration will only be influential in vessels where the stenosis detec-

tion algorithm is active. Thus the smoothness of the input data is an important determinant of sensitivity. However, by weighting the sensitivities by the uncertainty according to Eqs. (18) and (19) we found that the stenosis threshold, θ_s , is the most influential parameter with σ'_x , ζ and θ_h following thereafter. These parameters were then estimated by separating vessels used in the optimization procedure into two different cohorts. The filter and stenosis detection parameters θ_s , σ'_x and θ_s were estimated from cases with high variance related to stenosis threshold θ_s . The parameter ζ was estimated in a cohort of cases where θ_s contributed little variance. Optimal parameters were found by minimizing the difference between pressure drops calculated by using the 3D modeling framework and the 1D–0D model. Few studies have focused on estimating an appropriate velocity profile shape, ζ , in Eq. (3) in coronary arteries by means of 3D solutions.² Though such a profile is commonly assumed in studies focusing on pulse wave propagation, values such as $\zeta = 2$, Pouseille flow, or $\zeta = 9$, a plug-like shape,^{44,52} are commonly used. For the cases considered, we found that the optimal value was $\zeta = 4.31$, which is between both values reported in the literature.

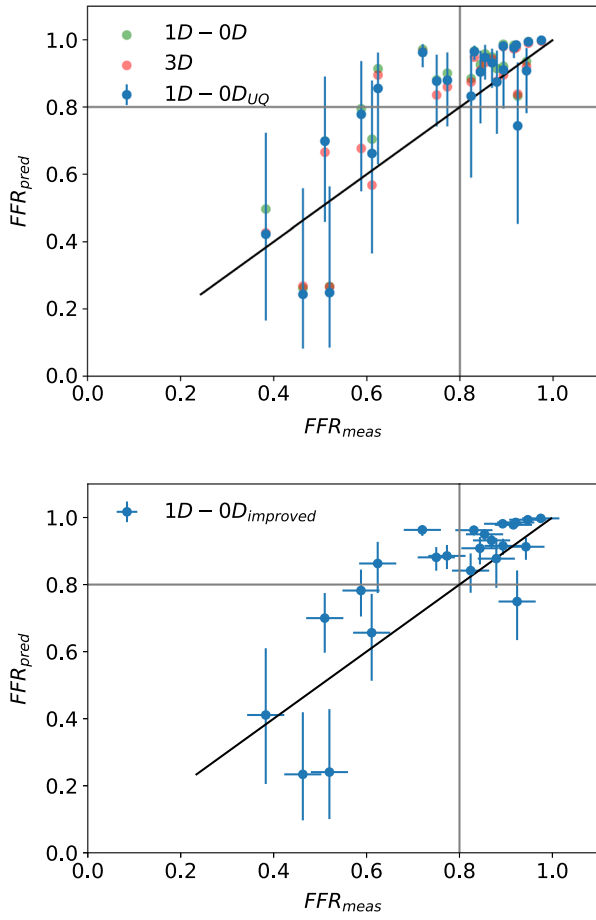


FIGURE 5. The mean predicted FFR, $E[Y]$, vs. invasive FFR. The vertical error bars represent the 95% prediction intervals. The top part of the figure represents the impact of all input parameters with assumed uncertainties as described in the “UQ&SA for FFR Prediction Setting” section, whereas all input parameters related to flow (CO , λ_{cor} and α) are fixed at their nominal values in the bottom figure. Here we also include the uncertainty in FFR (horizontal lines) represented as ± 2 standard deviations (std. dev. = 0.02) of repeated FFR measurements.²⁰

Furthermore, through the analysis of residuals between ΔP_{3D} and ΔP_{1D-0D} , we were able to differentiate between errors resulting from poor choices of parameters in the construction of the reduced-order model, and cases where the applied models no longer hold. We acknowledge that the 1D equations are not valid at stenotic regions, and account for this by identifying and replacing such regions with stenoses models. However, the model we employed was developed based on experiments on idealized stenotic geometries,⁵³ and as proven, has limited validity in severely calcified stenoses with non-cylindrical shape and abrupt changes in radius. Future work should focus on accounting for such 3D effects. Moreover, one can expect that the stenosis detection algorithm will not detect stenoses in the case of diffuse CAD, especially in cases where the transition from healthy to

stenotic areas is smooth and the stenotic region is very long. Although one might argue that in such a case, the main contribution to the pressure drop across the stenosis will be due to viscous losses, which are included in any case in the reduced-order model, the performance of the proposed method on a population of patients with diffusive CAD is of relevance and will be addressed in future work.

FFR predictions obtained using the reduced-order 1D-0D model, employing optimized parameters, are compared with FFR predictions obtained using the 3D framework with equivalent inlet and outlet boundary conditions, see Fig. 3. General agreement was satisfactory, with a bias of $FFR_{3D} - FFR_{1D-0D} = -0.03$ and a standard deviation of 0.03. Moreover, it is worth noting that the mismatch between both modeling approaches is normally significantly smaller than uncertainties in FFR prediction due to FFR model setup (CO , α , etc.), see Fig. 3. This suggests that even if the 1D-0D model output does not perfectly match 3D model output, it might lead to more accurate FFR predictions by allowing to explore FFR model parameters more extensively in order to design modeling setups that result in reduced uncertainty. Also predicted FFR errors with respect to measured FFR can be reduced because the lower computational cost of the 1D-0D model with respect to the 3D modeling framework might allow improved FFR modeling assumptions due to the increased capacity to explore such assumptions.

UQ&SA of Predicted FFR

We characterized FFR prediction uncertainty based on uncertainty of clinical measurements (CO , MAP), and assigning conservative estimates for unmeasured inputs (α , λ_{cor} , H , c). Geometric uncertainty was also included in terms of variations on minimum stenosis radius r_s and stenosis length L_s .

The hyperemic factor α was the most influential parameter for the assumed input uncertainties and modeling framework. α Represents the effect of adenosine on total coronary resistance, i.e. the factor by which peripheral resistance is reduced from baseline to hyperemic conditions. However, it is the corresponding increase of blood flow, CFR , which is important. Figure 6 shows the predicted mean values of CFR vs. the predicted mean values of FFR. The error bars represent the ranges for the 95% prediction interval. The mean value of CFR was 2.55 with a standard deviation of 0.54, in agreement with values reported in Refs. 21 and 49. It is worth mentioning that the same α is used for all vessels, probably increasing the sensitivity of predicted FFR to this parameter. In fact, it is expected that tissue located distal of a stenosis has a

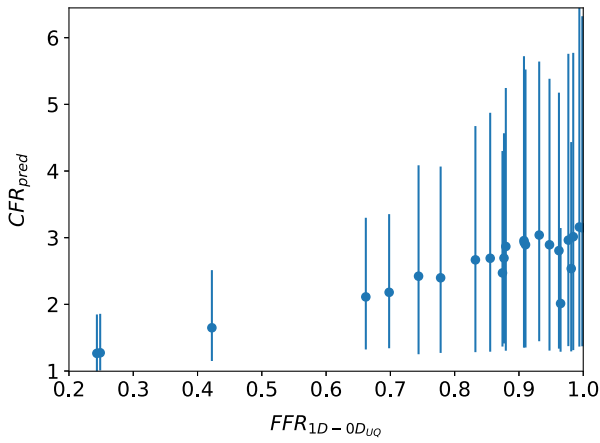


FIGURE 6. The mean predicted CFR vs. mean predicted FFR. The error bars represent the 95% prediction intervals for CFR.

reduced vasodilatory capacity. It is also evident from Fig. 4 that the influence of α varies substantially from case to case. As can be seen from Fig. 6, cases with low FFR values (i.e. severe stenoses) exhibit a lower increase in flow for the same value of α . Also, since α reduces total resistance, flow will tend to be redirected towards regions with small epicardial resistance.

The uncertainty about stenosis segmentation, represented by Δr_s in this study, also plays a relevant role in terms of its contribution to overall FFR prediction uncertainty. This is especially evident when the sensitivity indices are weighted by the variance of predicted FFR. However, our results show that the influence of Δr_s is smaller for lesions within the critical FFR range between 0.7 and 0.9. This indicates that both the variance of predicted FFR and the influence of geometry is higher for low FFR cases, i.e. cases with severe stenoses. This is also evident when comparing the standard deviation of Δr_s when the full set of measurements and the subset of measurements are used. This gives promise to computational FFR as a diagnostic tool which is meant to distinguish borderline cases.

Hematocrit is a parameter that affects both density and viscosity in our model. The influence of hematocrit is non-negligible when considering averaged sensitivity indices, however, once the indices are weighted by the variance, its influence diminishes. Thus hematocrit only has a noteworthy effect in cases with low or moderate uncertainty in FFR, which indicates that literature values for hematocrit/viscosity/density are sufficiently accurate for FFR prediction.

It is worth noting that most important parameters in terms of sensitivity and uncertainty of FFR predictions are all ultimately related to the definition of flow through the coronary tree (CO, λ_{cor} and α), which points to the fact that being able to model this variable correctly is of crucial importance for obtaining precise and reliable

FFR predictions. Figure 5 illustrates the achievable reduction in uncertainty if flow could be measured accurately in hyperemia, with particular impact in the critical FFR range between 0.7 and 0.9. Although the velocity of blood in epicardial arteries may be estimated with transthoracic Doppler echocardiography,¹⁶ currently such an approach has not been used in the context of model-based FFR prediction, and consequently there is no evidence to determine whether it can provide useful information or not. In any case, our results show that obtaining accurate estimates for flow is an aspect on which to focus in order to reduce prediction uncertainty and increase accuracy of model-based FFR prediction. Progress in this direction has been reported in Ref. 13.

Limitations and Future Work

It must be noted that we have modeled the geometrical uncertainty in a simplified manner in terms of global parameters affecting all stenotic regions. Further assessment of the role of uncertainty in segmented geometries should consider such factors over the entire geometry and not only at stenoses, by adopting an approach similar to the one reported in Ref. 5. Focus should also be directed towards quantifying such uncertainty, e.g. by considering segmentations based on different imaging modalities and performed by different observers.

In this work we have chosen to perform the UQ&SA for the FFR prediction setting described in the “UQ&SA for FFR Prediction Setting” section on all clinically measured locations. We have chosen this despite the fact that some patients had more than one measurement. However, correlated FFR predictions are generally expected only in the case of sequential measurements in the same vessel. The only case where one might expect substantial correlation is for FFR IDs 1 and 2 (see Table 12), which are taken along the same vessel. Moreover, it might be the case that two measurements along the same vessel yield very different FFR values, since *a priori* one can not exclude the presence of lesions between the two locations.

Available 3D simulation results contain detailed information about velocity profiles for the coronary trees and flow regimes under examination. A natural way to proceed would have been to investigate whether one can define a velocity profile coefficient, ζ that depends on local geometric features as well as the specific flow regime under consideration. In this first work we preferred to adopt a *one-fits-all* approach. Such a choice was motivated because of evident practical reasons, but also by the fact that we preferred to perform such a study once more patients become available. Similarly, the parameters involved in stenosis detection were chosen with a *one-size-fits-all* approach

as we expect that the variabilities of individual stenosis geometries to be mostly independent of individual patient characteristics.

APPENDIX 1: REDUCED-ORDER MODEL: FROM A 3D DOMAIN TO A 1D NETWORK

After centerline generation, the portions of the centerlines which coincide with arterial junctions were masked in order to exclude them from the 1D domain definition, since no reasonable 1D description of such portions of the domain can be formulated. We used the VMTK scripts ‘vmtkbranchextractor’ and ‘vmtkcenterlinemerge’ to obtain the topology of the 1D network. The first script uses definitions on what is treated as bifurcations in order to split the centerline into segments. The second script connects centerlines at a single point at bifurcations.¹ However, we did not find that these methods sufficiently split the domain into 1D segments, i.e. normally too little is considered as junction, see left part of Fig. 8. And thus additional processing was performed as described below. Points in mother (m) and daughter vessels (d) were masked based on different criteria. Points $p_{d,1}$ and $p_{d,2}$ in daughter vessel 1 and daughter vessel 2 were considered as part of the junction if

$$S_{d_1-d_2} \leq r_{\max\text{-sphere},d_1} + r_{\max\text{-sphere},d_2}, \quad (21)$$

where $S_{d_1-d_2}$ is the distance between points $p_{d,1}$ and $p_{d,2}$ and $r_{\max\text{-sphere},d_1}$ and $r_{\max\text{-sphere},d_2}$ are the maximum inscribed sphere radius at points $p_{d,1}$ and $p_{d,2}$ respectively. A point p_m of the mother vessel was considered as part of the junction if

$$S_{m-d} \leq 1.5 r_{\max\text{-sphere},d_m}, \quad (22)$$

where S_{m-d} is the distance between point p_m and a point, p_d in a daughter vessel. The value $r_{\max\text{-sphere},d_m}$ for a point p_d situated n points downstream of the center of the junction is found by evaluating $r_{\max\text{-sphere}}$ for all

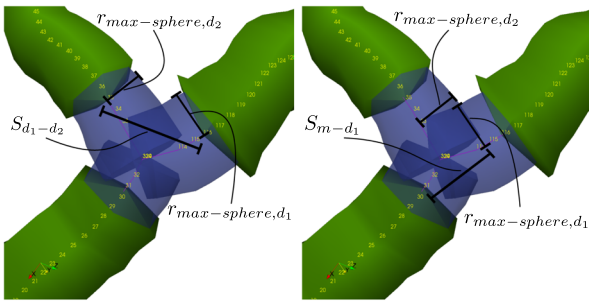


FIGURE 7. Illustration of step 1 for detection of junctions. The green tubes correspond to radius obtained from cross-sectional area perpendicular to centerline, and blue tubes to the radius of the maximum inscribed sphere.

daughter vessels at the same number of points downstream the center of the junction, and taking the minimum observed value, see Fig. 7. The criteria in Eqs. (21) and (22) were designed to keep as much of the 1D–0D domain intact; however, this caused incomplete masking in some cases (particularly of centerline points in daughter vessels) as visualized in Fig. 8. In order to check for the smoothness of transition from junctions to 1D segments we calculated the ratio of the maximum inscribed sphere and radius of the cross-sectional area, $r_i = \sqrt{\frac{A_i}{\pi}}$ for successive points, i.e.

$$\gamma = \frac{\frac{r_i}{r_{\max\text{-sphere},i}}}{\frac{r_{i+1}}{r_{\max\text{-sphere},i+1}}}. \quad (23)$$

After the initial junction mask in step 1, γ was calculated for the next 10 downstream centerline points in daughter vessels. If γ exceeded a value of 1.3 for a centerline point, $i = n$, the centerline points $1, \dots, n$, $n < 10$ were also marked as part of the junction. γ represents the ratio of the maximum inscribed sphere and the radius of the cross-sectional area for successive points. As noted earlier, this value is normally high in the transition from a bifurcation to an arterial segment. However this value may also be relatively high at the start/end of non cylindrical segments. Having observed values of up to approximately 1.3 in such regions, we used this value as a threshold. If we had used a lower value, non cylindrical segments could be misinterpreted as part of junctions. Figure 8 show the result before (left) and after (right) the correction.

APPENDIX 2: 3D MODELING FRAMEWORK: MODEL SETTING AND RESULTS

Mathematical Model

We consider the domain defined by the coronary tree vessels as $\Omega_f \in \mathbb{R}^3$. Moreover, its boundary is

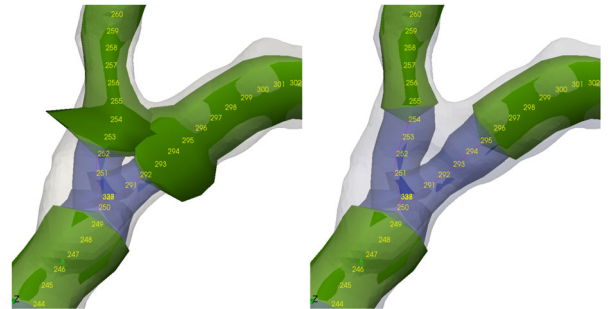


FIGURE 8. Illustration of the second step for masking of junctions. The left panel illustrates the result of applying junction criteria based on Eqs. (21) and (22), whereas the right panel shows the final result after correcting with criteria based on Eq. (23).

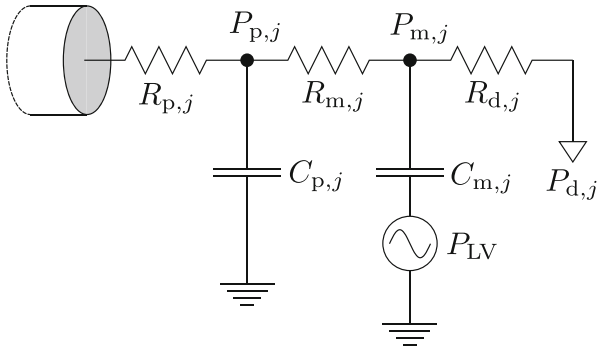


FIGURE 9. Schematic representation of a lumped-parameter model coupled to the j th 3D domain outlet $\Gamma_{out,j}^{out}$, shown in grey, and related to Eqs. (25) and (26). Portion of the 3D domain is also shown. C is compliance, R is resistance and P is pressure. Moreover, subscripts p, m and d stand for proximal, medial and distal, respectively. P_{LV} represents the time-varying left ventricular pressure.

partitioned as $\partial\Omega_f := \Gamma_{in} \cup \Sigma \cup \Gamma_{out}$, where Σ represents the wall boundary, Γ_{in} is the inlet cross-section and $\Gamma_{out} = \bigcup_{j=1}^{N_{out}} \Gamma_{out,j}$ is the union of the N_{out} outlets of the tree. Furthermore, blood flow in coronary arteries is modeled assuming that blood is an incompressible Newtonian fluid, for which the incompressible Navier–Stokes equations hold. These equations, along with boundary conditions are given by

$$\begin{cases} \frac{\partial \mathbf{u}}{\partial t} + \mathbf{u} \cdot \nabla \mathbf{u} = -\frac{1}{\rho} \nabla p + \nu \nabla^2 \mathbf{u} & \text{in } \Omega_f, \\ \nabla \cdot \mathbf{u} = 0 & \text{in } \Omega_f, \\ \mathbf{u} = \mathbf{0} & \text{on } \Sigma, \\ p = P_{in}(t) & \text{on } \Gamma_{in}, \text{ and} \\ p = P_{out,j}(t) & \text{on } \Gamma_{out,j}, j = 1, 2, \dots, N_{out}, \end{cases} \quad (24)$$

where $\rho = 1.05 \text{ g/cm}^3$ is the blood density and ν is the kinematic viscosity, given by $\nu = \mu/\rho$, with blood viscosity $\mu = 0.035P$. Furthermore, $P_{in}(t)$ is a prescribed pressure function and $P_{out,j}(t)$ is provided by the lumped-parameter model that is coupled to the j th outlet. Coronary arteries experience increased impedance during systole due to the contraction of the myocardium and increased pressure in the left ventricle. To account for this effect each outlet is coupled to a lumped-parameter model,²⁴ which in turn derives from the original work by Mantero *et al.*²⁷ This lumped-parameter model setup is depicted in Fig. 9 and the variation of volume V of each compartment is governed by the ordinary differential equations (ODEs)

$$\begin{cases} \frac{dV_{p,j}}{dt} = Q_{out,j} - \frac{P_{p,j} - P_{m,j}}{R_{m,j}}, \\ \frac{dV_{m,j}}{dt} = \frac{P_{p,j} - P_{m,j}}{R_{m,j}} - \frac{P_{m,j} - P_{d,j}}{R_{d,j}}. \end{cases} \quad (25)$$

Here, P and R represent pressure and resistance of different elements of the lumped model. Moreover,

subscripts p, m and d stand for proximal, medial and distal, respectively. Volumes relate to pressure *via* compliance C by the following relation

$$\begin{cases} P_{p,j} = \frac{V_{p,j}}{C_{p,j}}, \\ P_{m,j} = \frac{V_{m,j}}{C_{m,j}} + P_{LV}, \end{cases} \quad (26)$$

where P_{LV} is the left ventricular pressure.

Flow $Q_{out,j}$, for the j th outlet, is computed as

$$Q_{out,j} = \int_{\Gamma_{out,j}} \mathbf{u} \cdot \mathbf{n}_{out,j} dS, \quad (27)$$

where $\mathbf{n}_{out,j}$ is the exterior unit-vector normal for $\Gamma_{out,j}$. On the other hand, $P_{out,j}$ is provided by the lumped-parameter model as

$$P_{out,j} = P_{p,j} + R_{p,j} Q_{out,j}. \quad (28)$$

Numerical Methods

The mathematical models presented in the “**Mathematical Model**” section are solved using the open-source library CBCFLOW,¹¹ based on FEniCS.²⁶ In particular, CBCFLOW provides a flexible problem setup, allowing to combine its highly efficient incompressible Navier–Stokes solver with typical boundary conditions and simple models used in computational hemodynamics. Here, a Python script allowed CBCFLOW to interact with lumped-parameter models and to prescribe the needed boundary conditions.

The problem defined by Eq. (24) is solved by CBCFLOW using the Incremental Pressure Correction Scheme, described in Ref. 43. The computational mesh is composed of tetrahedral elements. The velocity field is approximated using piecewise-quadratic polynomials, while linear polynomials are used for pressure. The solver implementation follows very closely the one reported in Ref. 30. Apart from spatial and temporal discretization, the only numerical parameter to be set for this scheme is a multiplicative factor for the streamline diffusion stabilization term, referred to as s in this work, see Ref. 55 for details about this term. Moreover, Eq. (25) are solved using an explicit Euler discretization. Numerical parameters are set to $\Delta t = 1 \text{ ms}$ and $s = 1$. A parameter independence study has shown that such choices provide parameter independent FFR predictions for a set of patient-specific geometries.

Definition of Main Parameters from Patient-Specific Simulations

The flow to the coronary branch is based on the work of Sakamoto *et al.*,³⁷ who studied the dependence

of flow on coronary branch dominance. From this we calculate the relative distribution of total coronary flow, γ_k^j , to each coronary branch j for k dominant vasculature ($j = \{\text{right branch, left branch}\}$ and $k = \{\text{left dominance, right dominance}\}$). Furthermore, total coronary flow was assumed to be 4.5% of CO. Thus, the baseline coronary flow to a specific branch is

$$q_{\text{cor}} = 0.045 \cdot \gamma_k^j \cdot \text{CO}. \quad (29)$$

The two flow fractions may be combined to get the fraction of CO to a branch, $\lambda_{\text{cor}} = 0.045 \cdot \gamma_k^j$.

Total peripheral compliance is computed as a percentage of total arterial compliance of 1.7 mL mmHg.³² The percentage of the total arterial compliance assigned to the left/right branch is equal to the relation between flow in branch of interest over total CO, that is

$$C_{\text{tot}} = q_{\text{cor}} / \text{CO} \times 1.7 \text{ mL mmHg}, \quad (30)$$

MAP, pulse pressure (PP) and cardiac cycle duration (T) are extracted from pressure tracings for aortic pressure acquired during invasive FFR measurement. MAP is computed by time-averaging the pressure signal over a cardiac cycle. MAP and PP are used to prescribe a scaled characteristic aortic pressure waveform at the network's inlet and a scaled characteristic left ventricle pressure waveform (peak left ventricle pressure is 1.05 times the peak inlet pressure) for all lumped-parameter models. We chose to use a characteristic waveform as opposed to the measured waveform since the latter is not perfectly periodic and a corresponding left ventricle pressure waveform would then have to be estimated/fitted. The characteristic waveforms, taken from Ref. 24, are shown in Fig. 10.

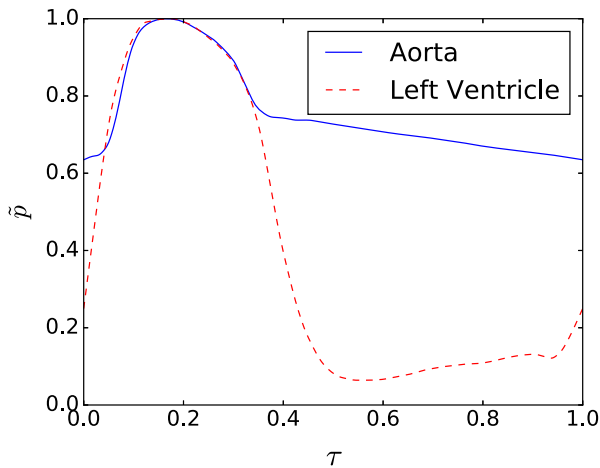


FIGURE 10. Aortic and left ventricle characteristic waveforms used for patient-specific simulations. τ and \tilde{p} are normalized time and pressure. The waveform shapes were taken from Ref. 24.

Total peripheral resistance for a given branch is estimated from MAP and the target branch flow in baseline conditions q_{cor}^j as

$$R_{\text{tot}} = \frac{\text{MAP} - P_d}{q_{\text{cor}}^j}, \quad (31)$$

where $P_d = 5$ mmHg is the outflow/venous pressure.

The total peripheral resistance R_{tot} and total peripheral compliance C_{tot} are distributed among outlets using Murray's law,³¹ that is

$$R_j = \frac{\sum_{i=1}^{N_{\text{out}}} r_i^3}{r_j^3} R_{\text{tot}} \quad (32)$$

and

$$C_j = \frac{r_j^3}{\sum_{i=1}^{N_{\text{out}}} r_i^3} C_{\text{tot}}, \quad (33)$$

where j stands for the j th outlet of the network. R_j and C_j have to be subsequently distributed among the different compartments (see Fig. 9) of the lumped-parameter model attached to the j th outlet. The fractions for distributing R_j among $R_{p,j}$, $R_{m,j}$ and $R_{d,j}$ are set to 0.01, 0.84 and 0.15, respectively. Similarly, fractions used to distribute C_j among $C_{a,j}$ and $C_{m,j}$ are 0.025 and 0.975, respectively. Parameter distribution among components of lumped-parameter models were empirically determined to obtain diastolic coronary flow rate waveforms with appropriate pulsatility.

Modeling Pipeline

The modeling pipeline is as follows

- (1) Using parameters defined in the previous section as initial guess, total peripheral resistance R_{tot} for a given branch is modified in order to match target branch flow q_{cor} defined by Eq. (29). The iterative procedure is described later in this section.
- (2) We determine heart rate, MAP and PP from pressure tracings taken under hyperemic conditions. Moreover, we use R_{tot} from previous step to estimate a new total peripheral resistance, now in hyperemic conditions: $R_{\text{tot,hyp}} = R_{\text{tot}}/\alpha$, which is subsequently distributed among outlets with criteria specified in Eq. (32). The hyperemic factor, α , was set to 3.
- (3) Steady state simulations are performed prescribing MAP at the inlet and replacing the lumped-parameter model by a single resistance at each outlet, where such resistance is $R_j = R_{p,j} + R_{m,j} + R_{d,j}$, as for the transient case.

Solution Monitoring and Total Resistance Estimation

As noted previously, total peripheral resistance R_{tot} is modified in order to match average branch flow q_{cor} defined in Eq. (29). Starting with the initial guess provided by Eq. (31), R_{tot} is updated after each cardiac cycle using

$$R_{\text{tot}}^{m+1} = R_{\text{tot}}^m (1 - \omega(q_{\text{cor}} - q_{\text{obs}})/q_{\text{cor}}), \quad (34)$$

where m is the iteration index (which corresponds to the cardiac cycle index), q_{cor} is the target coronary flow in a branch, provided by Eq. (29) and q_{obs} is the observed flow at the branch inlet. ω is a relaxation parameter and was set to $\omega = 0.9$. Once a new value for R_{tot} is available, the resistance is distributed among outlets using Eq. (32).

In order to compute predicted FFR, we have to extract average pressure values from 3D solutions. To do so we first define the subdomain

$$\Omega_{f,k} := \{\mathbf{x} \in \Omega_f : \|\mathbf{x} - \mathbf{x}_k\| < r_k\}, \quad (35)$$

where \mathbf{x}_k is the k -th node of a vessel's centerline that corresponds to the point where the invasive FFR measurement was taken, and r_k is the radius of the vessel at node k . Locations \mathbf{x}_k were identified by inspection of angiograms and segmentation results by modelers and cardiologists. Next, average pressure (over space and time) is computed as

$$\bar{P}_k = \frac{1}{T\Omega_{f,k}} \int_T \int_{\Omega_{f,k}} p \, d\Omega \, dt. \quad (36)$$

3D Simulation Results

While the primary objective of this work is to present and analyze a 1D-0D framework for model-based FFR

prediction, we report here the comparison of predicted FFR values obtained using the 3D modeling framework described in B vs. invasively measured FFR values. Such values are provided in order to show that the FFR prediction modeling framework, while still under development, provides results that are aligned with many publications on model-based FFR prediction. The average error of FFR predictions was -0.033 and the standard deviation of the error was 0.119 . Moreover, the correlation coefficient of predicted FFR vs. invasive FFR was 0.84 . In terms of diagnostic accuracy, prediction sensitivity, specificity, positive predicted value and negative predicted value were 60% , 93% , 86% and 76% , respectively. Figure 11 shows a scatter plot and a Bland-Altman plot for predicted FFR vs. measured FFR. More relevant for the current study are results reported in Fig. 12, that shows predicted FFR based on steady state simulations vs. predicted FFR based on transient simulations. In this case, mean error was -0.004 and standard deviation of the error was 0.003 , with a correlation coefficient of 1.00 .

APPENDIX 3: UQ&SA FRAMEWORK

We summarize the framework used by treating the patient specific model as a function M that predicts $y = M(\mathbf{z})$ based on input data \mathbf{z} . As the input data is uncertain it is represented as a random variable \mathbf{Z} which implies that prediction Y is also an uncertain random variable. We employ the nonintrusive UQ&SA methods of Monte Carlo and polynomial chaos to characterize the distribution of Y given the distribution of \mathbf{Z} . This is achieved by evaluating M at many samples drawn from the distribution of \mathbf{Z} , i.e. $y = M(\mathbf{z})$ at each sample point in $\{\mathbf{z}^{(s)}\}_{s=1}^{N_s}$. Eck *et al.*⁹

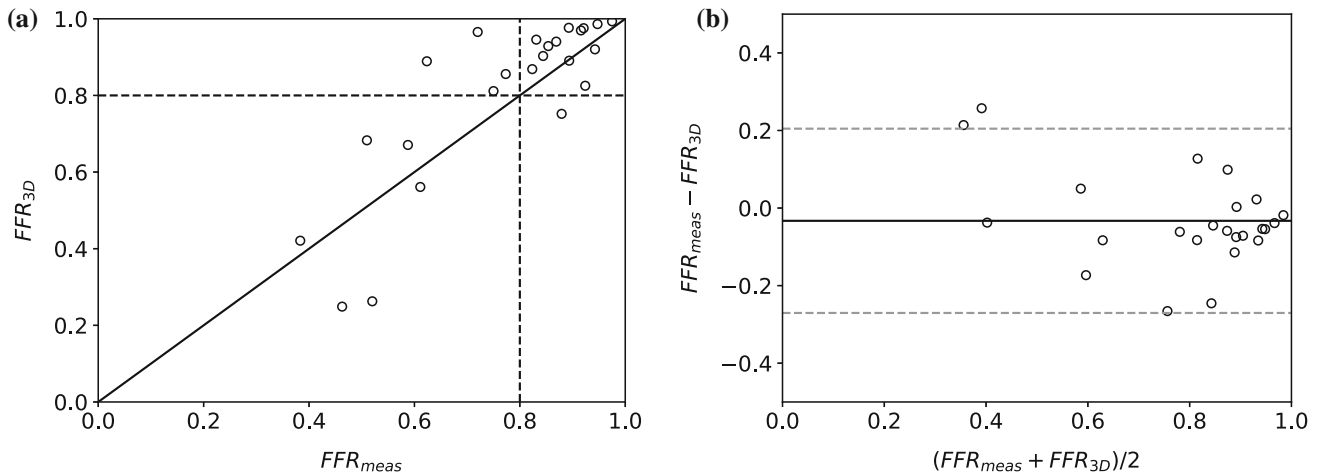


FIGURE 11. Predicted FFR, FFR_{3D} , vs. invasive FFR, FFR_{meas} . Scatter plot with grey line showing the FFR cutoff value of 0.8 (left) and Bland-Altman plot with dashed lines showing ± 2 standard deviations (right).

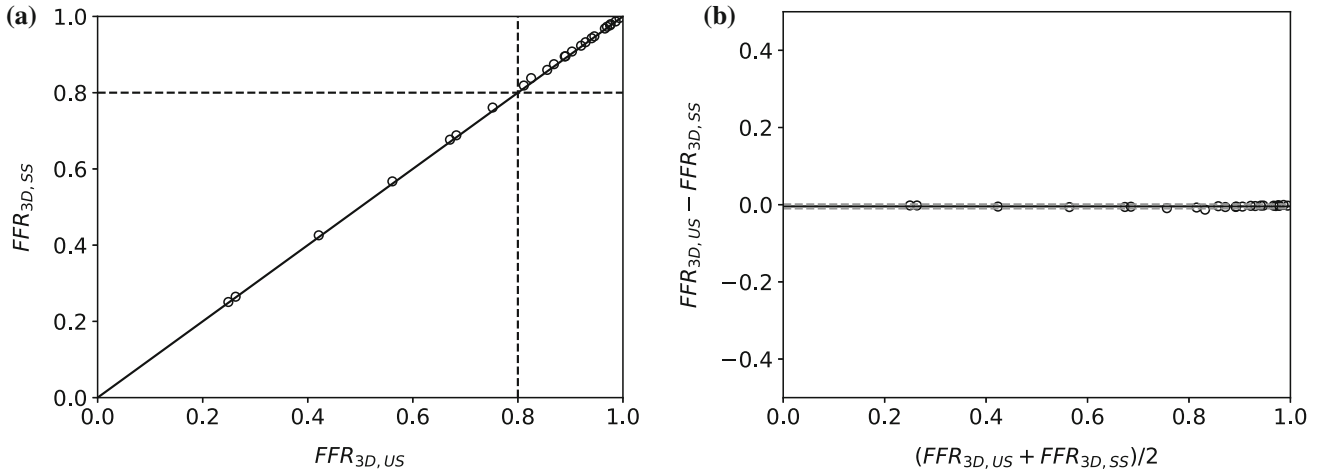


FIGURE 12. Predicted FFR based on steady state simulations, $FFR_{3D,SS}$, vs. predicted FFR based on transient simulations, $FFR_{3D,US}$. Scatter plot with grey line showing the FFR cutoff value of 0.8 (left) and Bland–Altman plot with dashed lines showing ± 2 standard deviations (right).

present several methods and concepts of UQ&SA within the context of cardiovascular modeling, and we refer the reader to this work for more details regarding the methods of UQ&SA used here.

The uncertainty of Y is fundamentally due to the uncertainty of \mathbf{Z} propagated through the model M . Thus it is critical to employ a distribution of \mathbf{Z} that reflects the conditions the UQ&SA is intended to analyze. To assess performance of a patient specific model the input distribution must reflect the actual uncertainties present in clinical procedures and population variation. However, UQ&SA may also be employed to analyze a model's range of behavior and to identify parameters relevant for estimation from measured values of y . In this case the distribution of \mathbf{Z} should reflect the range of plausible values for the inputs. Typically, only a range of values is considered and no prior knowledge is available to prioritize certain regions, thus a uniform distribution is appropriate to investigate the model's dependence on the parameters.

Once the approximate distribution of Y is available from the UQ&SA procedure various measures of uncertainty of Y are available such as statistical moments or quantiles of Y . These quantities are of primary interest when assessing model performance, however, SA augments this by assessing the portion of uncertainty due to particular inputs, allowing prioritization of efforts to reduce uncertainty. In this context, Sobol sensitivity indices, first-order (S_i) and total ($S_{T,i}$), are widely employed,³⁹ and defined as

$$S_i = \frac{\mathbb{V}[\mathbb{E}[Y | Z_i]]}{\mathbb{V}[Y]}, \quad (37a)$$

$$S_{T,i} = 1 - \frac{\mathbb{V}[\mathbb{E}[Y | \mathbf{Z}_{-i}]]}{\mathbb{V}[Y]}, \quad (37b)$$

where the vector, \mathbf{Z}_{-i} , contains all elements of \mathbf{Z} except Z_i . These indices partition the total $\mathbb{V}[Y]$ into portions attributable to specific combinations of inputs. The first order indices S_i quantify the variance due to Z_i alone, i.e. independent of the values of the other inputs. The total sensitivity index, $S_{T,i}$, includes effect due to interaction with other parameters and represents the reduction in variance expected to be achieved by fixing Z_i at a particular value.

Larger values of S_i suggest that Z_i strongly affects Y and thus may be a prime target for improved measurement or optimization in the context of parameter estimation. In the case where $S_{T,i}$ and thus also S_i are small, Z_i has little influence on Y and should not be prioritized for improved measurement and may not be estimated accurately in an inverse problem context. When S_i is small but $S_{T,i}$ is large, the effect of Z_i depends greatly on the values of other parameters thus it may still be valuable to improve its measurement, and it may be estimated in an inverse problem though its identifiability may depend on the values of other parameters.

TABLE 11. Patient-specific data for the 13 patients considered in this work.

Patient IDs	Sex (–)	Age (years)	Height (cm)	Weight (kg)	MAP (mmHg)	CO (L/min)
1	Female	58	162.0	78.0	95.7	3.8
2	Female	67	157.0	64.0	83.7	4.1
3	Male	36	183.0	95.0	92.7	6.2
4	Male	47	172.0	92.0	99.7	5.5
5	Male	60	175.0	92.0	109.7	4.9
6	Male	61	186.0	92.0	109.7	4.3
7	Male	47	183.0	105.0	123.7	5.4
8	Male	70	182.0	87.0	103.3	4.6
9	Female	50	175.0	80.0	100.3	6.3
10	Male	59	176.0	102.0	101.3	5.3
11	Female	76	163.0	55.0	98.7	3.4
12	Male	59	188.0	90.0	97.0	4.9
13	Male	58	178.0	84.0	88.7	6.0

For a description of data acquisition see “[Study Population](#)” section.

TABLE 12. Data for invasive FFR measurements and quantitative coronary angiography for the 13 patients considered in this work.

FFR IDs	Patient IDs	Lesion location	QCA	FFR	Prox. pres. (mmHg)	Dist. pres. (mmHg)	Heart rate (1/min)
1	1	LAD	74.0*	0.52	100.0	52.0	85.7
2	1	LAD	74.0*	0.46	121.0	56.0	83.9
3	1	LCX	48.0	0.88	116.0	102.0	81.6
4	2	LAD	23.0	0.92	79.0	73.0	61.2
5	2	LAD	30.0	0.81	78.0	63.0	70.2
6	3	LAD	17.0	0.87	84.0	73.0	94.5
7	4	RCA	62.0	0.89	94.0	84.0	108.1
8	5	LAD	32.0	0.83	77.0	64.0	89.6
9	5	LAD diagonal	13.0	0.84	77.0	65.0	94.5
10	5	RPDA	11.0	0.94	87.0	82.0	76.4
11	6	RCA	12.0	0.89	112.0	100.0	88.2
12	7	LAD	5.0	0.97	80.0	78.0	69.8
13	7	LAD diagonal	38.0	0.95	95.0	90.0	67.0
14	7	RCA	24.0	0.92	76.0	70.0	67.0
15	8	LAD	37.0	0.75	84.0	63.0	51.3
16	8	RCA	37.0	0.85	89.0	76.0	58.5
17	9	LCX	65.0	0.38	120.0	46.0	74.1
18	10	RCA	48.0	0.59	97.0	57.0	91.6
19	10	LAD	39.0	0.61	90.0	55.0	86.3
20	10	LCX	78.0	0.51	102.0	52.0	82.8
21	11	LAD	16.0	0.92	107.0	98.0	66.7
22	12	LAD	59.0	0.62	85.0	53.0	80.0
23	12	RCA	54.0	0.82	102.0	84.0	80.5
24	13	LAD	47.0	0.77	97.0	75.0	99.2
25	13	LCX	63.0	0.72	100.0	72.0	87.0

*Same lesion refers to FFR measurements 1 and 2. Quantitative coronary angiography (QCA) is a measure of the percent diameter stenosis degree, obtained by inspection of angiography images.

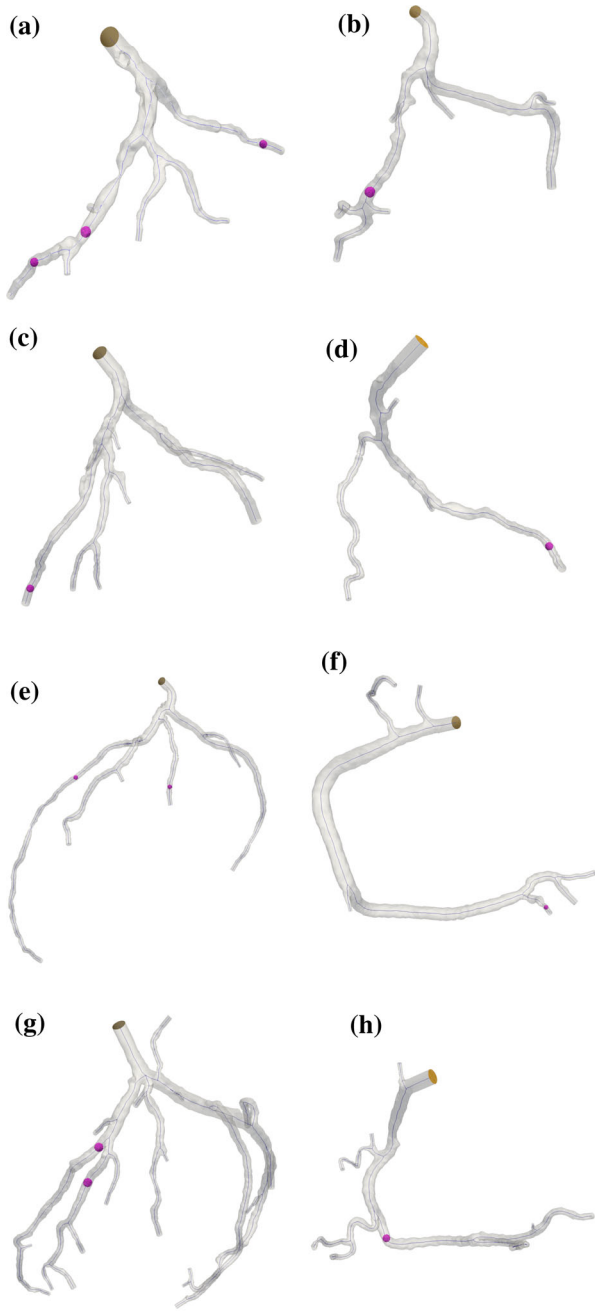


FIGURE 13. Visualization of 3D domain for some of the patients included in the study (see figure sub-captions for details). Magenta sphere is where distal pressure P_{distal} was evaluated in 3D domains using Eq. (36). Branch inlet, where proximal pressure P_{proximal} is prescribed is highlighted in orange. The centerline used as reduced-order model domain is evidenced in blue. (a) Patient 1, left branch (b) Patient 2, left branch (c) Patient 3, left branch (d) Patient 4, right branch (e) Patient 5, left branch (f) Patient 5, right branch (g) Patient 7, left branch (h) Patient 7, right branch.

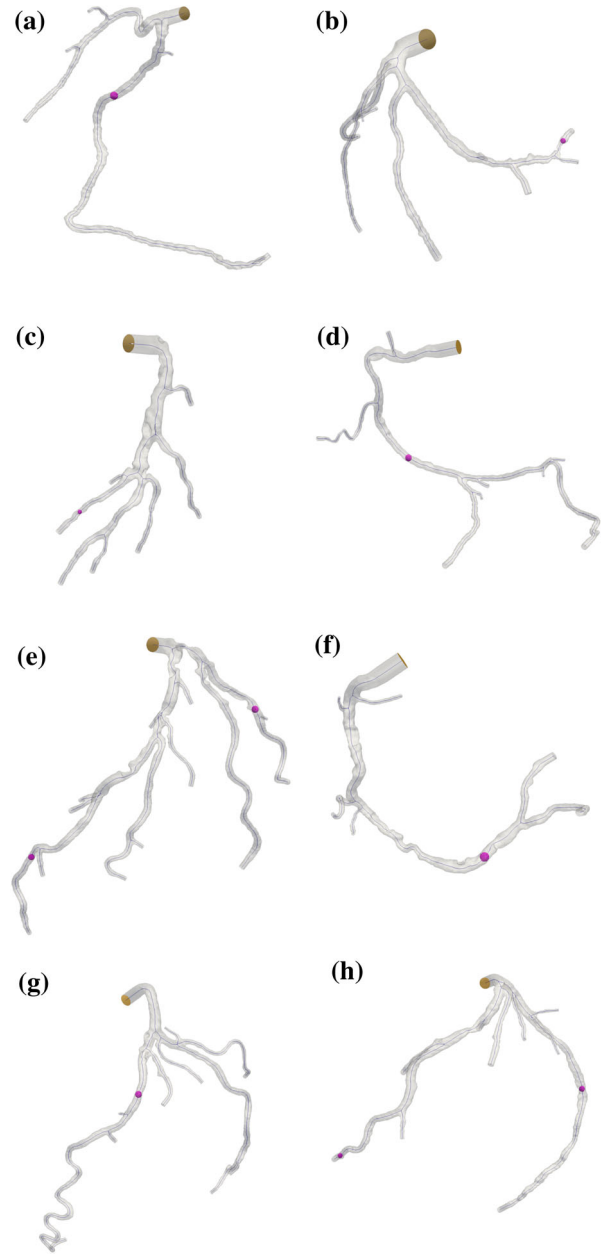


FIGURE 14. Visualization of 3D domain for some of the patients included in the study (see figure sub-captions for details). Magenta sphere is where distal pressure P_{distal} was evaluated in 3D domains using Eq. (36). Branch inlet, where proximal pressure P_{proximal} is prescribed is highlighted in orange. The centerline used as reduced-order model domain is evidenced in blue. (a) Patient 6, right branch (b) Patient 9, left branch (c) Patient 8, left branch (d) Patient 8, right branch (e) Patient 10, left branch (f) Patient 10, right branch (g) Patient 11, left branch (h) Patient 13, left branch.

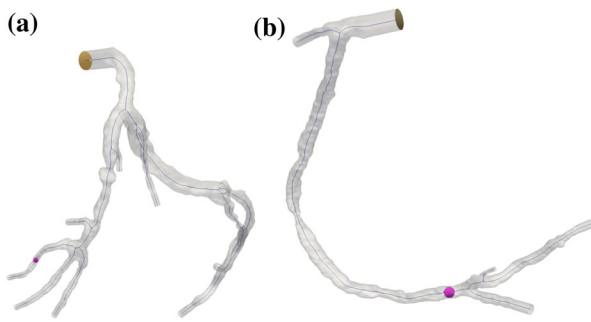


FIGURE 15. Visualization of 3D domain for some of the patients included in the study (see figure sub-captions for details). Magenta sphere is where distal pressure P_{distal} was evaluated in 3D domains using Eq. (36). Branch inlet, where proximal pressure P_{proximal} is prescribed is highlighted in orange. The centerline used as reduced-order model domain is evidenced in blue. (a) Patient 12, left branch (b) Patient 12, right branch.

APPENDIX 4: PATIENT-SPECIFIC DATA AND INVASIVE MEASUREMENTS

Table 11 shows patient characteristics and non-invasive measurements for all patients considered in this work. Furthermore, Table 12 shows data obtained during invasive angiography, and include stenosis location, quantitative coronary angiography (QCA), cardiac cycle averaged pressure proximal and distal to the stenosis, and heart rate. QCA is a measure of the percent diameter stenosis degree obtained by inspection of angiography images. Figures 13, 14 and 15 shows visualizations of all 3D domains for the patients considered in this work, where we have highlighted the locations of distal measurements with (magenta) spheres, and the branch inlets (orange) where proximal measurements were obtained.

ACKNOWLEDGMENTS

This work was partially supported by NTNU Health (Strategic Research Area at the Norwegian University of Science and Technology) and by The Liaison Committee for Education, Research and Innovation in Central Norway. Computational resources in Norwegian HPC Infrastructure were granted by the Norwegian Research Council by Project Nr. NN9545K. LRH was partly funded by a Peder Sather Grant: Mainstreaming Sensitivity Analysis And Uncertainty Auditing.

CONFLICT OF INTEREST

There are no conflicts of interest.

ETHICAL APPROVAL

All procedures performed in studies involving human participants were in accordance with the ethical standards of the Institutional and/or National Research Committee and with the 1964 Helsinki Declaration and its later amendments or comparable ethical standards.

INFORMED CONSENT

Informed consent was obtained from all individual participants included in the study.

REFERENCES

- Antiga, L., M. Piccinelli, L. Botti, B. Ene-Iordache, A. Remuzzi, and D. A. Steinman. An image-based modeling framework for patient-specific computational hemodynamics. *Med. Biol. Eng. Comput.* 46(11):1097–1112, 2008. <http://link.springer.com/10.1007/s11517-008-0420-1>.
- Blanco, P. J., C. A. Bulant, L. O. Müller, G. D. M. Talou, C. G. Bezerra, P. L. Lemos, and R. A. Feijóo. Comparison of 1D and 3D models for the estimation of fractional flow reserve. *arXiv:1805.11472* [physics] (2018). *ArXiv: 1805.11472*.
- Boileau, E., S. Pant, C. Roobottom, I. Sazonov, J. Deng, X. Xie, and P. Nithiarasu. Estimating the accuracy of a reduced-order model for the calculation of fractional flow reserve (FFR). *Int. J. Numer. Methods Biomed. Eng.* 34(1):e2908, 2018. <http://doi.wiley.com/10.1002/cnm.2908>.
- Bråten, A. T., and R. Wiseth. Diagnostic Accuracy of CT-FFR Compared to Invasive Coronary Angiography with Fractional Flow Reserve—Full Text View—ClinicalTrials.gov (2017). <https://clinicaltrials.gov/ct2/show/NC03045601>.
- Brault, A., L. Dumas, and D. Lucor. Uncertainty quantification of inflow boundary condition and proximal arterial stiffness coupled effect on pulse wave propagation in a vascular network. 2016, arXiv preprint. *arXiv:1606.06556*.
- Cook, C. M., R. Petraco, M. J. Shun-Shin, Y. Ahmad, S. Nijjer, R. Al-Lamee, Y. Kikuta, Y. Shiono, J. Mayet, D. P. Francis, S. Sen, and J. E. Davies. Diagnostic accuracy of computed tomography-derived fractional flow reserve: a systematic review. *JAMA Cardiol.* 2017. <http://cardiology.jamanetwork.com/article.aspx?doi=10.1001/jamacardio.2017.1314>.
- De Bruyne, B., N. H. Pijls, B. Kalesan, E. Barbato, P. A. Tonino, Z. Piroth, N. Jagic, S. Möbius-Winkler, G. Rioufol, N. Witt, P. Kala, P. MacCarthy, T. Engström, K. G. Oldroyd, K. Mavromatis, G. Manoharan, P. Verlee, O. Frobert, N. Curzen, J. B. Johnson, P. Jüni, and W. F. Fearon. Fractional flow reserve-guided PCI versus medical therapy in stable coronary disease. *N. Engl. J. Med.* 367(11), 991–1001, 2012. <http://www.nejm.org/doi/abs/10.1056/NEJMoa1205361>.
- Dubin, J., D. C. Wallerson, R. J. Cody, and R. B. Devoreux. Comparative accuracy of Doppler echocardiographic methods for clinical stroke volume determination.

- Am. Heart J.* 120(1):116–123, 1990. <http://www.sciencedirect.com/science/article/pii/000287039090168W>.
- ⁹Eck, V. G., W. P. Donders, J. Sturdy, J. Feinberg, T. Delhaas, L. R. Hellevik, and W. Huberts. A guide to uncertainty quantification and sensitivity analysis for cardiovascular applications. *Int. J. Numer. Methods Biomed. Eng.* 2015. <http://onlinelibrary.wiley.com/doi/10.1002/cnm.2755/abstract>.
- ¹⁰Eck, V. G., J. Sturdy, and L. R. Hellevik. Effects of arterial wall models and measurement uncertainties on cardiovascular model predictions. *J. Biomech.* 2016. <http://www.sciencedirect.com/science/article/pii/S0021929016312210>.
- ¹¹Evju, Ø., and M. S. Alnæs. CBCFLOW. Bitbucket Repository. 2017.
- ¹²Feinberg, J., and H. P. Langtangen. Chaospy: an open source tool for designing methods of uncertainty quantification. *J. Comput. Sci.* 11:46–57, 2015. <https://doi.org/10.1016/j.jocs.2015.08.008>.
- ¹³Fiorentini, S., L. M. Saxhaug, T. G. Bjastad, and J. Avdal. Maximum velocity estimation in coronary arteries using 3D tracking Doppler. <https://doi.org/10.1109/TUFFC.2018.2827241>.
- ¹⁴Gaur, S., K. A. Øvrehus, D. Dey, J. Leipsic, H. E. Bøtker, J. M. Jensen, J. Narula, A. Ahmadi, S. Achenbach, B. S. Ko, E. H. Christiansen, A. K. Kaltoft, D. S. Berman, H. Bezerra, J. F. Lassen, and B. L. Nørgaard. Coronary plaque quantification and fractional flow reserve by coronary computed tomography angiography identify ischaemia-causing lesions. *Eur. Heart J.* 37(15), 1220–1227, 2016. <https://academic.oup.com/eurheartj/article-lookup/doi/10.1093/eurheartj/ehv690>.
- ¹⁵Hannawi, B., W. W. Lam, S. Wang, and G. A. Younis. Current use of fractional flow reserve: a nationwide survey. *Tex. Heart Inst. J.* 41(6):579–584, 2014. <https://doi.org/10.14503/THIJ-13-3917>.
- ¹⁶Holte, E.: Transthoracic Doppler Echocardiography for the Detection of Coronary Artery Stenoses and Microvascular Coronary Dysfunction. NTNU, 2017. <http://brage.bibsys.no/xmlui/handle/11250/2486248>.
- ¹⁷Hunyor, S. N., J. M. Flynn, and C. Cochineas. Comparison of performance of various sphygmomanometers with intra-arterial blood-pressure readings. *Br. Med. J.* 2(6131):159–162, 1978. <http://www.ncbi.nlm.nih.gov/pmc/articles/PMC1606220/>.
- ¹⁸Huo, Y., and G. S. Kassab. Intraspecific scaling laws of vascular trees. *J. R. Soc. Interface* 9(66), 190–200, 2012. <https://doi.org/10.1098/rsif.2011.0270>.
- ¹⁹Itu, L., P. Sharma, V. Mihalef, A. Kamen, C. Suciu, and D. Lomaniciu. A patient-specific reduced-order model for coronary circulation. In: 2012 9th IEEE International Symposium on Biomedical Imaging (ISBI). IEEE, 2012, pp. 832–835. http://ieeexplore.ieee.org/xpls/abs_all.jsp?arnumber=6235677.
- ²⁰Johnson, N. P., D. T. Johnson, R. L. Kirkeeide, C. Berry, B. De Bruyne, W. F. Fearon, K. G. Oldroyd, N. H. J. Pijls, and K. L. Gould. Repeatability of fractional flow reserve despite variations in systemic and coronary hemodynamics. *JACC Cardiovasc. Interv.* 8(8):1018–1027, 2015. <http://www.sciencedirect.com/science/article/pii/S1936879815006998>.
- ²¹Johnson, N. P., R. L. Kirkeeide, and K. L. Gould. Is discordance of coronary flow reserve and fractional flow reserve due to methodology or clinically relevant coronary pathophysiology? *JACC Cardiovasc. Imaging* 5(2):193–202, 2012. <https://doi.org/10.1016/j.jcmg.2011.09.020>.
- ²²Jones, E., T. Oliphant, P. Peterson, et al. SciPy: open source scientific tools for Python (2001–). <http://www.scipy.org/>.
- ²³Kenner, T.: The measurement of blood density and its meaning. *Basic Res. Cardiol.* 84(2):111–124, 1989. <http://link.springer.com/article/10.1007/BF01907921>.
- ²⁴Kim, H. J., I. E. Vignon-Clementel, J. S. Coogan, C. A. Figueroa, K. E. Jansen, and C. A. Taylor. Patient-specific modeling of blood flow and pressure in human coronary arteries. *Ann. Biomed. Eng.* 38(10):3195–3209, 2010. <http://s://doi.org/10.1007/s10439-010-0083-6>.
- ²⁵Liang, F., K. Fukasaku, H. Liu, and S. Takagi. A computational model study of the influence of the anatomy of the circle of Willis on cerebral hyperperfusion following carotid artery surgery. *Biomed. Eng. Online* 10:84, 2011. <https://doi.org/10.1186/1475-925X-10-84>.
- ²⁶Logg, A., K. A. Mardal, and G. Wells, eds. Automated Solution of Differential Equations by the Finite Element Method. Lecture Notes in Computational Science and Engineering, vol. 84. Berlin: Springer, 2012. <https://doi.org/10.1007/978-3-642-23099-8>.
- ²⁷Mantero, S., R. Pietrabissa, and R. Fumero. The coronary bed and its role in the cardiovascular system: a review and an introductory single-branch model. *J. Biomed. Eng.* 14(2):109–116, 1992. <http://linkinghub.elsevier.com/retrieve/pii/014154259290015D>.
- ²⁸Matsuda, J., T. Murai, Y. Kanaji, E. Usui, M. Araki, T. Niida, S. Ichijyo, R. Hamaya, T. Lee, T. Yonetsu, M. Isobe, and T. Kakuta. Prevalence and clinical significance of discordant changes in fractional and coronary flow reserve after elective percutaneous coronary intervention. *J. Am. Heart Assoc.* 2016. <https://doi.org/10.1161/JAHA.116.004400>.
- ²⁹Morris, P. D., D. A. Silva Soto, J. F. Feher, D. Rafiroiu, A. Lungu, S. Varma, P. V. Lawford, D. R. Hose, and J. P. Gunn. Fast virtual fractional flow reserve based upon steady-state computational fluid dynamics analysis. *JACC Basic Transl. Sci.* 2(4):434–446, 2017. <http://linkinghub.elsevier.com/retrieve/pii/S2452302X17301353>.
- ³⁰Mortensen, M., and K. Valen-Sendstad. Oasis: a high-level/high-performance open source Navier–Stokes solver. *Comput. Phys. Commun.* 188:177–188, 2015. <http://linkinghub.elsevier.com/retrieve/pii/0010465514003786>.
- ³¹Murray, C. D. The physiological principle of minimum work. *Proc. Natl Acad. Sci. USA* 12(3):207–214, 1926. <http://www.ncbi.nlm.nih.gov/pmc/articles/PMC1084489/>.
- ³²Otsuki, T., S. Maeda, M. Iemitsu, Y. Saito, Y. Tanimura, R. Ajisaka, and T. Miyauchi. Systemic arterial compliance, systemic vascular resistance, and effective arterial elastance during exercise in endurance-trained men. *Am. J. Physiol. Regul. Integr. Comp. Physiol.* 295(1):R228–R235, 2008. <http://www.physiology.org/doi/10.1152/ajpregu.00009.2008>.
- ³³Pijls, N. H., W. F. Fearon, P. A. Tonino, U. Siebert, F. Ikeno, B. Bornschein, M. van't Veer, V. Klauss, G. Manoharan, T. Engström, K. G. Oldroyd, P. N. Ver Lee, P. A. MacCarthy, and B. De Bruyne. Fractional flow reserve versus angiography for guiding percutaneous coronary intervention in patients with multivessel coronary artery disease. *J. Am. Coll. Cardiol.* 56(3):177–184, 2010. <http://linkinghub.elsevier.com/retrieve/pii/S0735109710016025>.
- ³⁴Ri, K., K. K. Kumamaru, S. Fujimoto, Y. Kawaguchi, T. Dohi, S. Yamada, K. Takamura, Y. Kogure, N. Yamada, E. Kato, R. Irie, T. Takamura, M. Suzuki, M. Hori, S.

- Aoki, and H. Daida. Noninvasive computed tomography-derived fractional flow reserve based on structural and fluid analysis: reproducibility of on-site determination by unexperienced observers. *J. Comput. Assist. Tomogr.* 1, 2017. <http://Insights.ovid.com/crossref?an=00004728-90000000-99330>.
- ³⁵Robert, C. P., and G. Casella. Monte Carlo Statistical methods, 2nd edn., Softcover Reprint of the Hardcover 2, 2004 edn. Springer Texts in Statistics. New York: Springer, 2010.
- ³⁶Rogers, G., and T. Oosthuyse. A comparison of the indirect estimate of mean arterial pressure calculated by the conventional equation and calculated to compensate for a change in heart rate. *Int. J. Sports Med.* 21(02):90–95, 2000. <https://www.thieme-connect.com/products/ejournals/html/10.1055/s-2000-8865?update=true#R616-17>.
- ³⁷Sakamoto, S., S. Takahashi, A. U. Coskun, M. I. Papafaklis, A. Takahashi, S. Saito, P. H. Stone, and C. L. Feldman. Relation of distribution of coronary blood flow volume to coronary artery dominance. *Am. J. Cardiol.* 111(10):1420–1424, 2013. <http://linkinghub.elsevier.com/retrieve/pii/S000291491300386X>.
- ³⁸Saltelli, A.: Making best use of model evaluations to compute sensitivity indices. *Comput. Phys. Commun.* 145(2):280–297, 2002. [https://doi.org/10.1016/S0010-4655\(02\)00280-1](https://doi.org/10.1016/S0010-4655(02)00280-1).
- ³⁹Saltelli, A.: Global Sensitivity Analysis: The Primer. Chichester Wiley, 2008. <http://catalog.lib.ncsu.edu/record/NCSU2123570>.
- ⁴⁰Sankaran, S., H. J. Kim, G. Choi, and C. A. Taylor. Uncertainty quantification in coronary blood flow simulations: impact of geometry, boundary conditions and blood viscosity. *J. Biomech.* 49(12):2540–2547, 2016. <http://www.sciencedirect.com/science/article/pii/S0021929016000117>.
- ⁴¹Schroeder, W. J., and K. M. Martin. The visualization toolkit. In: Visualization Handbook. Elsevier, 2005, , pp. 593–614. <http://linkinghub.elsevier.com/retrieve/pii/B9780123875822500320>.
- ⁴²Shahzad, R., H. Kirisli, C. Metz, H. Tang, M. Schaap, L. van Vliet, W. Niessen, and T. van Walsum. Automatic segmentation, detection and quantification of coronary artery stenoses on CTA. *Int. J. Cardiovasc. Imaging* 29(8):1847–1859, 2013. <https://doi.org/10.1007/s10554-013-0271-1>.
- ⁴³Simo, J., and F. Armero. Unconditional stability and long-term behavior of transient algorithms for the incompressible Navier–Stokes and Euler equations. *Comput. Methods Appl. Mech. Eng.* 111(1–2):111–154, 1994. <http://linkinghub.elsevier.com/retrieve/pii/0045782594900426>.
- ⁴⁴Smith, N., A. Pullan, and P. Hunter. An anatomically based model of transient coronary blood flow in the heart. *SIAM J. Appl. Math.* 62(3):990–1018, 2002. <https://epubs.siam.org/doi/abs/10.1137/S0036139999355199>.
- ⁴⁵Spaan, J. A. E.: Coronary blood flow. In: Developments in Cardiovascular Medicine, vol. 124. Dordrecht: Springer, 1991. <http://link.springer.com/10.1007/978-94-011-3148-3>.
- ⁴⁶Antiga, L., and S. Manini. The vascular modeling toolkit website. <https://www.vmtk.org>. Accessed 27 Oct 2017.
- ⁴⁷Sturdy, J., J. K. Kjernlie, H. M. Nydal, V. G. Eck, and L. R. Hellevik. Uncertainty of computational coronary stenosis assessment and model based mitigation of image resolution limitations (Forthcoming).
- ⁴⁸Tonino, P. A., B. De Bruyne, N. H. Pijls, U. Siebert, F. Ikeno, M. van't Veer, V. Klauss, G. Manoharan, T. Engström, K. G. Oldroyd, et al. Fractional flow reserve versus angiography for guiding percutaneous coronary intervention. *N. Engl. J. Med.* 360(3):213–224, 2009. <http://www.nejm.org/doi/full/10.1056/NEJMoa0807611>.
- ⁴⁹Uren, N. G., J. A. Melin, B. De Bruyne, W. Wijns, T. Baudhuin, and P. G. Camici. Relation between myocardial blood flow and the severity of coronary-artery stenosis. *N. Engl. J. Med.* 330(25):1782–1788, 1994. <https://doi.org/10.1056/NEJM199406233302503>.
- ⁵⁰Wongkrajang, P., W. Chinswangwatanakul, C. Mookkhamkukun, N. Chuangsuwanich, B. Wesarackitti, B. Thaowto, S. Laiwejpithaya, and O. Komkhum. Establishment of new complete blood count reference values for healthy Thai adults. *Int. J. Lab. Hematol.* <https://onlinelibrary.wiley.com/doi/abs/10.1111/ijlh.12843>.
- ⁵¹World Health Organization. Top 10 Causes of Death, 2018. <http://www.who.int/news-room/fact-sheets/detail/the-top-10-causes-of-death>.
- ⁵²Xiao, N., J. Alastruey, and C. Alberto Figueroa. A systematic comparison between 1-D and 3-D hemodynamics in compliant arterial models. *Int. J. Numer. Methods Biomed. Eng.* 30(2):204–231, 2014. <https://doi.org/10.1002/cnm.2598>.
- ⁵³Young, D. F., and F. Y. Tsai. Flow characteristics in models of arterial stenoses—I. Steady flow. *J. Biomech.* 6(4):395–410, 1973. <http://linkinghub.elsevier.com/retrieve/pii/0021929073900997>.
- ⁵⁴Yushkevich, P. A., J. Piven, H. C. Hazlett, R. G. Smith, S. Ho, J. C. Gee, and G. Gerig. User-guided 3D active contour segmentation of anatomical structures: significantly improved efficiency and reliability. *NeuroImage* 31(3):1116–1128, 2006. <http://linkinghub.elsevier.com/retrieve/pii/S1053811906000632>.
- ⁵⁵Zienkiewicz, O. C., R. L. Taylor, and P. Nithiarasu. The Finite Element Method for Fluid Dynamics, 7th edn. Oxford: Butterworth-Heinemann, 2014. OCLC: ocn869413341.